Experimental Study of the Flow Field in a Model Rotor-Stator Disk Cavity

Using Particle Image Velocimetry

by

Parag Pathak

A Thesis Presented in Partial Fulfillment
of the Requirements for the Degree
Master of Science

Approved February 2013 by the
Graduate Supervisory Committee:

Ramendra P. Roy, Chair
Ronald Calhoun
Taewoo Lee

ARIZONA STATE UNIVERSITY

May 2013

ABSTRACT

Modern day gas turbine designers face the problem of hot mainstream gas ingestion into rotor-stator disk cavities. To counter this ingestion, seals are installed on the rotor and stator disk rims and purge air, bled off from the compressor, is injected into the cavities. It is desirable to reduce the supply of purge air as this decreases the net power output as well as efficiency of the gas turbine. Since the purge air influences the disk cavity flow field and effectively the amount of ingestion, the aim of this work was to study the cavity velocity field experimentally using Particle Image Velocimetry (PIV).

Experiments were carried out in a model single-stage axial flow turbine set-up that featured blades as well as vanes, with purge air supplied at the hub of the rotor-stator disk cavity. Along with the rotor and stator rim seals, an inner labyrinth seal was provided which split the disk cavity into a rim cavity and an inner cavity. First, static gage pressure distribution was measured to ensure that nominally steady flow conditions had been achieved. The PIV experiments were then performed to map the velocity field on the radial-tangential plane within the rim cavity at four axial locations.

Instantaneous velocity maps obtained by PIV were analyzed sector-by-sector to understand the rim cavity flow field. It was observed that the tangential velocity dominated the cavity flow at low purge air flow rate, its dominance decreasing with increase in the purge air flow rate. Radially inboard of the rim cavity, negative radial velocity near the stator surface and positive radial velocity near the rotor surface indicated the presence of a recirculation region in the cavity

i

whose radial extent increased with increase in the purge air flow rate. Qualitative flow streamline patterns are plotted within the rim cavity for different experimental conditions by combining the PIV map information with ingestion measurements within the cavity as reported in Thiagarajan (2013).

To Baba

ACKNOWLEDGMENTS

TABLE OF CONTENTS

LIST OF TABLES

LIST OF FIGURES

x

xi

NOMENCLATURE

c_w non-dimensional mass flow rate of purge air, $= \dot{m}_{purge}/\mu R_h$

$c_{w,fd}$ nondimensional free disk pumping flow rate, $= 0.219 Re_\phi^{0.8}$

$c_{w,min}$ minimum purge flow rate required to completely seal the cavity

C_{vax} vane axial chord length

$\dot{m}_{purge}$ purge air mass flow rate

p instantaneous static gage pressure

$\bar{p}$ time-average static gage pressure

p_{atm} ambient pressure

r radial coordinate

R_h vane/blade hub radius

Re_{vax} main air flow Reynolds number, $= \rho V_{ax} C_{vax}/\mu$

Re_ϕ disk rotational Reynolds number, $= \rho \, \Omega R_h^2/\mu$

s axial gap between rotor and stator disks

V_{ax} mixed-mean axial velocity of main air in annulus

V_r local radial velocity of cavity fluid

V_ϕ local tangential velocity of cavity fluid

x distance from the rotor disk

β_2 angle, to axial direction downstream, of the main air velocity

relative to the blade – at just downstream of vane trailing edge (^{o})

δt laser pulse separation time

Greek Symbols

η local sealing effectiveness

θ $(90 - \phi)$

μ dynamic viscosity

ρ density of air

ϕ azimuthal coordinate

Ω rotor disk speed

Chapter 1

INTRODUCTION

1.1   Background

A gas turbine is a rotary engine which extracts work from a combusted gas. The three main features of a gas turbine are: a compressor, a combustion chamber and a turbine. The main flow air is first compressed before it is injected with fuel and the mixture is ignited. The resulting high temperature, high pressure gas is then expanded in a turbine, producing work. Higher turbine inlet temperatures lead to incrementally higher efficiencies. Over the years, the inlet temperatures have risen from 1000 K in 1940 (Whittle W1 engine) to around 1800 K at present. Such high temperatures, typically above the melting point of turbine metal components, have been possible due to advancement in material technology and the employment of effective sealing and cooling systems.

Figure 1.1 shows a typical turbine cross-section with sealing and cooling arrangements. The high-temperature mainstream gas while flowing over the vanes and the blades can penetrate into the wheel space (or disk cavity) between the rotor and the stator of a stage, this being especially true for high pressure stages. This phenomenon of transport of hot main gas into disk cavities is termed "ingestion" and leads to overheating of internal components, especially of the rotor disk, reducing their durability. To reduce ingestion, seals are provided at the rims of rotor disk and stator. Additionally, cooler air bled-off from the compressor discharge (purge air) is supplied to the cavities. The purge air maybe supplied

with or without pre-swirl at various locations ranging from the cavity hub to near the rim seals.

Nozzle Guide Vanes

Turbine Blades

Mainstream Gas

Turbine Rim Seal

Blade-Cooling Air

Pre-Swirl Nozzles

Stator

Disk Cavity

Disk Cavity Sealing/ Cooling Air

H.P. Turbine Rotor Disk

L.P. Turbine Rotor Disk
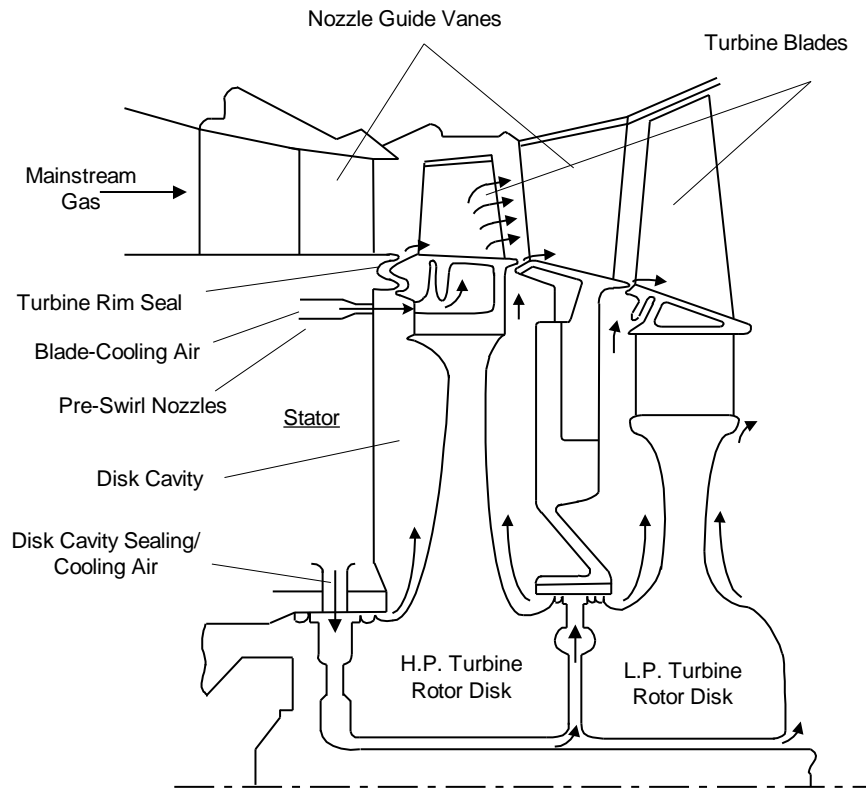
Fig. 1.1 A typical turbine cross-section with sealing and cooling air system (by courtesy of Wilson et al., 1995)

The amount of purge air used is an issue. Excessive purge air amount will lead to reduced overall gas turbine efficiency. On the other hand, inadequate supply of purge air will cause overheating of the turbine internals including the rotor disks and can result in damages. A sound understanding of the flow field in the mainstream gas path and in the disk cavity is an important step towards attaining the objective of optimal purge air use.

Simulation of these flow fields using three-dimensional unsteady computational fluid dynamics (CFD) codes has been an emerging trend, but it

requires validation. As such, bench-mark quality experiments in simplified laboratory turbine rigs are necessary.

1.2   Literature Survey

In this section, a brief survey of selected experimental, theoretical and computational studies is presented.

In one of the first investigations of the flow between rotating and stationary disks, Batchelor (1951) suggested the presence of separate boundary layers on the rotor and stator disks with a fluid core rotating between them. According to him, the stator boundary layer will have radial inflow of fluid which eventually mixes with the core fluid, is entrained into the rotor boundary layer, and then out of the system. For this type of flow, the turbulent flow structure in the cavity depends on the swirl ratio (β) and the turbulent flow parameter (λ_T), Owen and Rogers (1989).

Daily and Nece (1960) carried out pioneering experiments on rotor-stator disk cavities and classified the cavity flow on the basis of the rotational Reynolds number (Re_ϕ) and axial gap ratio (G) into four regimes, I through IV. Regimes I and II are laminar, whereas regimes III and IV are turbulent. Regime IV, featuring turbulent flow and separate boundary layers on the rotor and stator, is approximately bounded by $10^5 < Re_\phi < 10^7$ and $0.05 < G < 0.217$ and pertains to our experiments.

Bayley and Owen (1970) were among the first to present results on rotationally-induced ingestion in a shrouded rotor-stator system with superposed sealing air flow. They noted that the cavity pressure increased with increase in the

sealing air flow, reducing ingestion. Also, the seal clearance ratio (G_c), and not the gap ratio (G), was found to be the controlling parameter for the minimum mass flow rate, $c_{w,min}$, required to prevent ingestion.

Abe et al. (1979) conducted experiments in a rig featuring 27 vanes which turned the main flow by 50° along with a rotor disk with no blades. Various seal geometries were investigated via flow visualization, velocity, pressure and propane gas concentration measurements. It was proposed that the non-axisymmetry of the main flow caused by the vanes affected the pressure distribution inside the cavity. This formed the basis for future studies on ingestion caused by the mainstream annulus flow.

Phadke and Owen (1983 and 1988 a, b, c) performed experiments on several shroud geometries using flow visualization, as well as measurement of pressure and tracer gas concentration. Three mainstream flow cases were studied: quiescent (no flow), quasi-axisymmetric, and non-axisymmetric. In the quiescent mainstream flow experiments (1983), the radial clearance seals exhibited a pressure inversion effect at higher purge air flow rate; the wheelspace pressure increased with rotational speed, unlike the axial clearance seal case. This trend was later (1988 a) shown to be associated with the radially outward flow on the rotor impinging on the stator thereby creating a fluid curtain that helped prevent ingestion and rendered the radial clearance seal more effective than their axial clearance counterpart. A simple correlation was obtained for each of the seals for determining $c_{w,min}$ in terms of the shroud clearance and rotational speed. For the other two mainstream annulus flow cases, Phadke and Owen (1988 b, c)

4

suggested two flow regimes: a rotation-dominated regime at small values of Re_{vax}/Re_ϕ, and an external-flow-dominated regime at large values of the same. It was concluded that the externally induced ingestion was mainly affected by the circumferential pressure asymmetry.

Green and Turner (1994) were the first to perform experiments in a rotor-stator rig with vanes and blades and an axial clearance rim seal. Surprisingly, the full stage (i.e. with blades and vanes) showed reduced ingestion compared to the stage with only the vanes (i.e. no blades). This suggested that the rotor blades may have had an effect of smoothening out the pressure asymmetry caused by the vanes.

The physical mechanisms involved in the turbine rim seal ingestion process such as the vane/blade periodic pressure field and turbulent transport in the rim seal overlap region were discussed by Johnson et al. (1994). Large scale instabilities in some rotating flows were also showed to contribute to the ingestion process.

Gallier et al. (2000) carried out an experimental study of unsteady flow in the mainstream gas path and near the rim seal region using Particle Image Velocimetry. Measurements were performed at specific blade positions relative to the vanes in order to characterize the effect of the rotor potential field on the behavior of the flow emerging from the rim seal. The purge air flow was found to have a significant effect on the main gas path flow.

Gentilhomme et al. (2002) reported time-average pressure and ingestion measurements in a model single-stage axial flow turbine. Steady and unsteady

CFD simulations showed that the unsteady effects due to the rotor have a strong influence on the ingestion process.

Bohn et al. (2003) performed unsteady 2D Laser Doppler Velocimetry measurements in a model 1.5-stage turbine to study the velocity distribution in and inboard of the upstream cavity rim seal. It was observed that ingestion increased whenever a rotor blade passed a vane.

Cao et al. (2003) reported an experimental and CFD study of the interaction of the main gas path and rim sealing flows. The experiments were conducted in a model two-stage axial flow turbine rig with a simple axial gap between the rotor and stator disks. Unsteady flow structures in the rotor-stator gap near the rim were predicted by CFD and were thought to be associated with the interaction of the main annulus and cavity flows. A qualitative agreement was found between the unsteady pressure measurements and the corresponding unsteady CFD results.

Johnson et al. (2006) developed a theoretical model wherein the rim seal clearance was treated as an orifice. Time-averaged pressure distributions from two-dimensional time-dependent CFD calculations along with a lumped orifice discharge coefficient were used in the model to estimate the pressure-driven ingestion and egress. The model showed good agreement with the experimental results by Bohn et al. (2003). Later, Johnson et al. (2008) used steady, three-dimensional simulation and two different discharge coefficients, for ingestion and egress, to model ingestion. This model was compared with the experimental data from Arizona State University with good agreement.

Roy et al. (1999, 2000, 2005 and 2007) carried out experiments on a model single-stage axial turbine rig featuring blades, vanes, and seals on both rotor and stator rims. Time-averaged as well as unsteady static pressure measurements were obtained at various locations in the main gas path and the disk cavity. Tracer gas (CO_2) concentration measurements were performed at several radial and axial locations in the disk cavity. The PIV technique was employed to investigate the cavity flow field.

Zhou et al. (2011) reported experimental results for three rim cavity configurations of a model axial flow turbine stage with vanes, blades, and rim seals. The tracer gas (CO_2) method was employed to measure ingestion of mainstream gas into the disk cavity and the flow field within the cavity was mapped by PIV. Unsteady three-dimensional CFD simulation of a half stage sector was carried out for one of the rim seal configurations; it under predicted the measured ingestion. Circumferentially rotating low-pressure structures in the disk cavity typically predicted by full-360° three-dimensional unsteady CFD simulations were suggested as one of the reasons.

Wang et al. (2012) carried out unsteady three-dimensional full-360° CFD simulation of a model axial flow turbine stage and compared the results with the experimental data from the Arizona State University rig. Time-dependent pressure distribution in the main gas path showed irregular patterns which were attributed to the vane and blade flow interactions. The time-average circumferential pressure profiles in the main gas path were found to be in excellent agreement with the

7

experimental data. However, the measured tangential velocity distributions did not reach the high values predicted by the simulations.

1.3   Overview of Present Work

In this work, experiments were carried out in a model single-stage axial flow turbine rig with vanes, blades, and rim seals on both the rotor and stator, along with a labyrinth seal radially inboard in the disk cavity. Though simpler than an actual gas turbine stage, the model stage retained the important features which influence ingestion.

The remainder of the thesis is organized as follows:

Chapter 2 contains a description of the experimental facility, the turbine stage, the techniques and procedures followed for measuring the time-average static pressure in the main gas path and the disk cavity, and the instantaneous velocity field in the disk cavity.

Chapter 3 contains the experimental results and their discussion.

Finally, Chapter 4 summarizes the conclusions and provides some recommendations for future research.

Chapter 2

THE EXPERIMENTS

2.1   The Experimental Facility

The experimental facility shown in Figs. 2.1 and 2.2 has three major components – the main blower, the secondary blower, and the rotor. Each of these is described in detail below.

Main Blower

The mainstream air flow for the turbine is supplied by a centrifugal blower (22.4 kW, Hauck, TBA-20-30). The main blower can supply an air flow rate of up to 1.42 m^3/s ($\cong$ 3000 cfm) and is controlled by a variable-frequency motor drive (Cutler Hammer, AF 95). The single-stage turbine section of the rig is located on the suction side of the blower. The blower inlet is connected to a 292 mm (11.5") i.d. plexiglass circular duct via a diffuser with a divergence angle of 5°. The blower discharges to the ambient through an approximately 2.235 m (7' 4") long, 311 mm (12.25") i.d. vertical pipe connected to an exhaust duct.

Measurement of mainstream air flow rate

A pitot tube rake (United Sensor, USNH-N-107) is used to measure the mainstream air flow rate. The rake consists of five pitot tubes equally spaced along a manifold and is installed in the 292 mm i.d. plexiglass circular duct at approximately 0.984 m (3' 2.75") upstream of the main blower inlet. A digital manometer (Validyne, PS309, range: 0-2" water gage) is connected to the pitot tube rake to measure the dynamic pressure head, this being the difference between the stagnation pressure and the static pressure. The analog output from
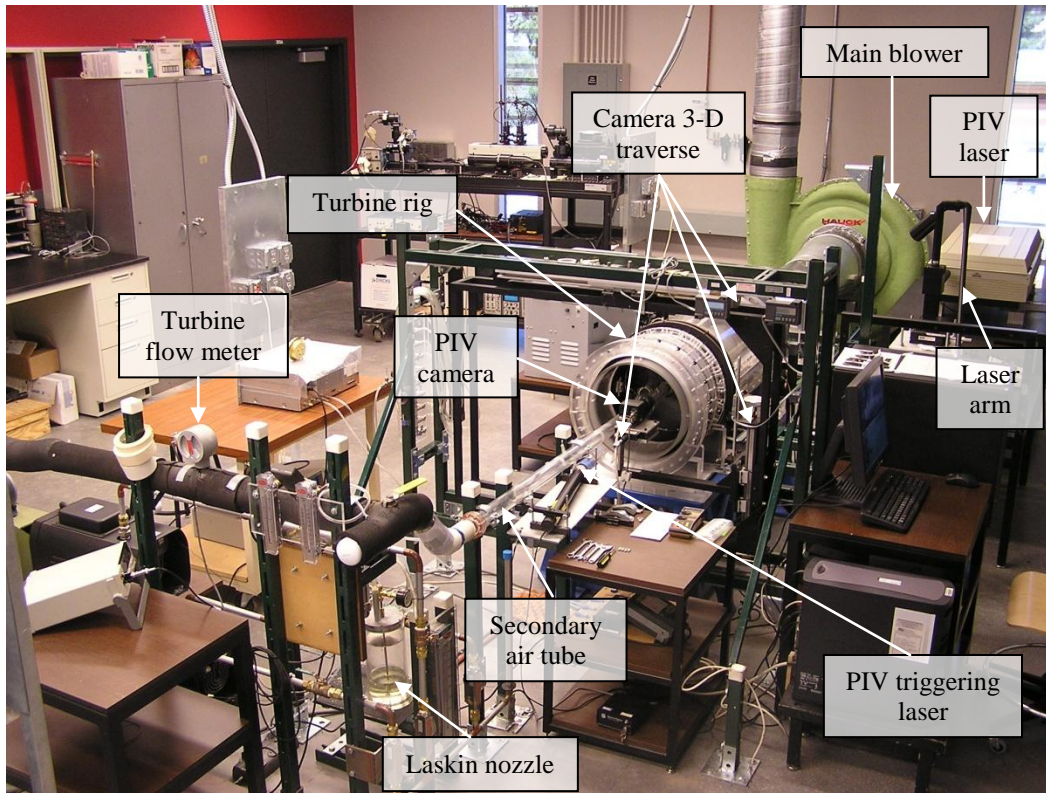
Fig. 2.1 Rotor-stator disk cavity rig with axial injection of purge air
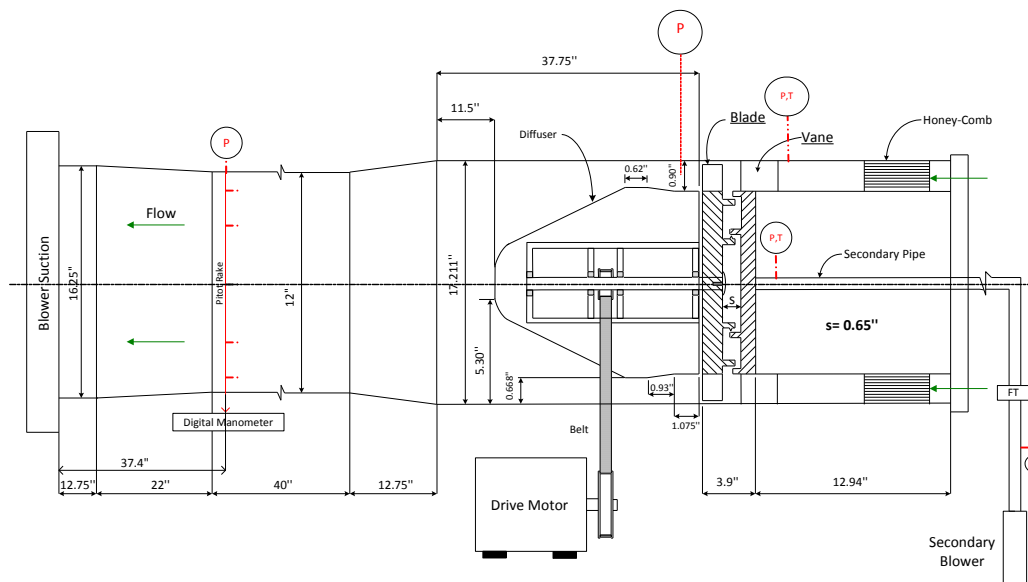
Fig. 2.2 Schematic of ASU Turbine rig

the digital manometer is routed to a data acquisition system (Analogic DATA6500) which displays the mean and RMS values of the dynamic pressure.

Secondary Blower

The purge air flow is provided by a smaller secondary centrifugal blower (2.24 kW, Hauck, TBA-16-3). This blower is also controlled by a variable-frequency motor drive (Emerson, Prism) and can provide an air flow rate of up to 0.12 m^3/s ($\cong$ 250 cfm). The discharge from the secondary blower flows through a 760 mm (29.9") long, 50.8 mm (2.0") nominal diameter insulated galvanized iron pipe; this ensures a well-developed flow upstream of a turbine flow meter installed downstream of the pipe. The purge air subsequently flows through a check valve to the hub of the disk cavity via a 1.780 m (5' 10.1") long, 38.1 mm (1.5") i.d. plexiglass pipe. To straighten the air flow, a honeycomb section (12.7 mm (0.5") long, 3.2 mm (0.126") hexagonal cell size) has been installed in the plexiglass secondary air pipe 1.600 mm (5' 3") upstream of the inlet to the disk cavity.

Measurement of the purge air flow rate

A turbine flow meter (EG&G Flow Technology, FT-32) is used to measure the purge air volumetric flow rate. The flow meter provides an analog voltage output that is routed to a digital multimeter (Model 45, Fluke) which converts the output voltage to the corresponding air flow rate via a calibration relation.

Rotor

The rotor disk, made of aluminum, is 31.8 mm (1.25") thick and 391.4 mm (15.4") in diameter. It is mounted on a 50.8 mm (2.0") diameter mild-steel shaft which is belt-driven by a 2.24 kW (3 HP), 1750 rpm max, GE motor. The step-up belt drive has a speed ratio of 3.27:1, allowing a maximum rotor speed of 5720 rpm. The motor speed is controlled by a 3.73 kW (5 HP) Eaton-Cutler Hammer adjustable frequency drive (AFD). The AFD helps maintain the rotor at particular rotational speeds during experiments. A digital photoelectric tachometer (Biddle Instruments, accuracy = ± 1 rpm) is used to measure the rotor speed.

During shutdown, a rapid deceleration of the motor may cause it to become a generator, this feeding energy back into the AFD. To counter this, the AFD has been equipped with a dynamic braking resistor (Power-Ohm Registors, P13549-405), rated at 2.8 kW at a total resistance of 65.0 Ω.

2.1.1 The Turbine Stage

The turbine stage shown in Fig. 2.3 is located on the suction side of the blower so that the disk cavity remains optically accessible from the radial as well as the axial direction. A 120.7 mm (4.75") long honeycomb section (Polypropylene, 0.315" cell size, black, Plascore, PP30-5) is provided in the annular main air passage 152.4 mm (6.0") upstream of the vane to straighten the incoming flow.

The plexiglass stator is 19.1 mm (0.75") thick and has a diameter of 391.4 mm (15.4"). There are 22 partial height, full length guide vanes which turn the mainstream air flow by 68.6°, thus applying a realistic swirl to the flow. The rotor
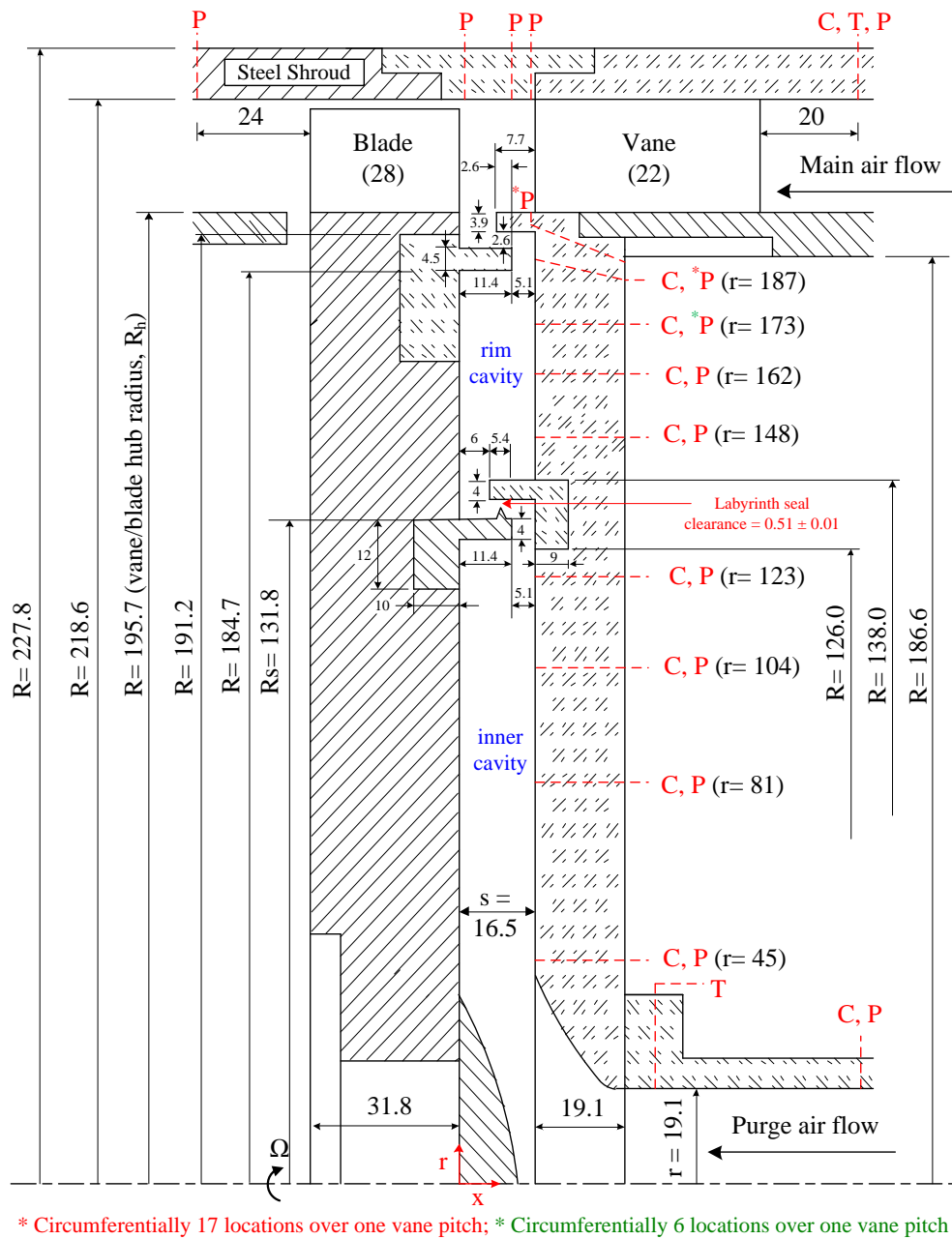
Fig. 2.3 Schematic diagram of the single-stage rim-seal arrangement (C: tracer gas concentration tap, P: time-average static pressure tap, T: thermocouple); all dimensions are in mm

13

disk is of the same diameter as the stator disk. The rotor has 28 partial height, partial length blades; the radial clearance between the blade tip and the steel outer shroud is 1.5 mm (0.059"). Given the main blower capacity, the partial blade and vane height allows the main air axial velocity in the annulus to be adequately high. The axial gap between the stator and rotor disks is maintained constant at 16.5 mm (0.65").

Rim and inner seal arrangement

Figure 2.3 shows the seal arrangement in the turbine stage. Rim seals are provided on the rotor and the stator disks; a labyrinth seal is also provided radially inboard. The rim seals have an axial overlap of 2.6 mm (0.102") and the same radial clearance. The labyrinth seal has a radial clearance of 0.51 mm ± 0.01 mm (0.020") and an axial overlap of 5.4 mm (0.212"). This divides the disk cavity into an *inner cavity* and a *rim cavity*.
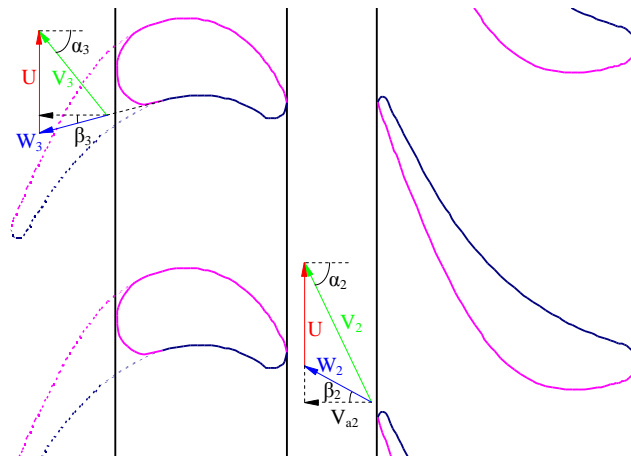
Fig. 2.4 Main air velocity triangles

Figure 2.4 shows the velocity triangle diagram of the main air at the vane exit. β_2 is the angle of the main air velocity relative to the blade (W_2) with respect

to the axial direction. A more useful estimate of β_2 would be at the entrance of the blade. A large and positive β_2 ensures that the rotor will operate as a turbine and this can be obtained with a low rotor speed and high main air flow rate. The low speeds of the rotor can be achieved by using the adjustable frequency drive and the braking resistor. The purge air supplied at the disk cavity hub exits the cavity into the main gas path through the rim seal gap and is known to affect the flow structure of the main air (Gallier et. al. 2000). However, the velocity triangle was unlikely to be altered as the maximum purge air flow rate in our experiments was only 2.1% of the lowest main air flow rate.

2.2   Time-Average Static Pressure Measurement

Time average static pressure measurement experiments were conducted initially to ensure that nominally steady state flow condition had been achieved. The experimental procedure and the instruments used for these measurements are described in brief here.
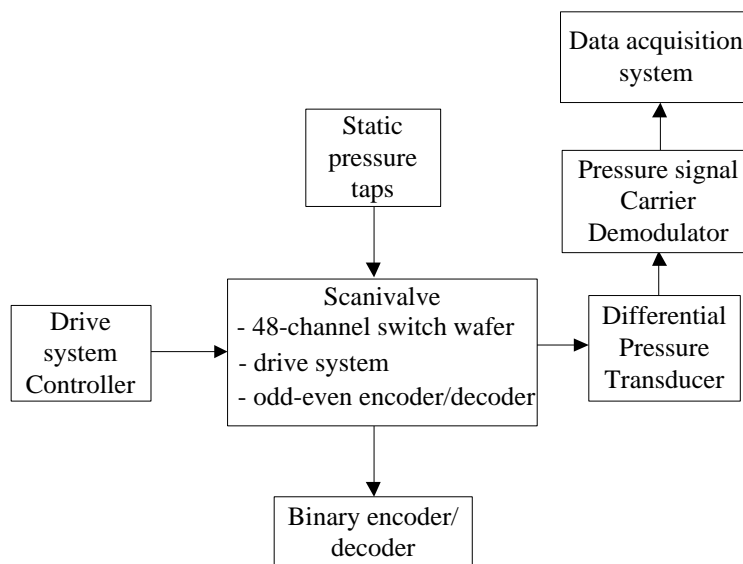
Fig. 2.5 The static pressure measurement system

The pressure measurement system, outlined in Fig. 2.5, consists of static pressure taps, a Scanivalve, a differential pressure transducer, a signal carrier demodulator and a data acquisition system.

2.2.1 System Components

Static pressure taps

Miniature bulged stainless steel tubulations (TUBN-063, 1.6 mm o.d., 1.0 mm i.d., Scanivalve Corp.), shown in Fig. 2.6, were used in the static pressure taps. Silicone rubber sealant was applied around the tubes at their interface with the plexiglass surface to prevent air leakage. It was also ensured that no machining burrs were present on the plexiglass near the pressure taps as this may have affected the measurements.
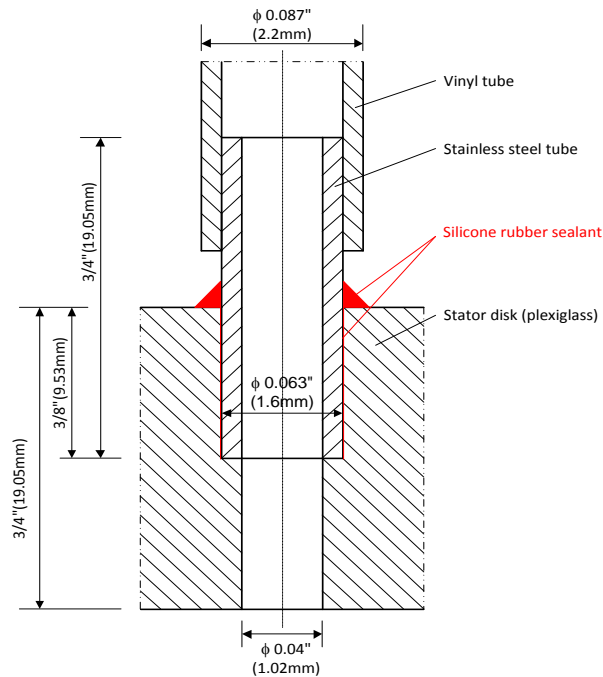
Fig. 2.6 Schematic of a static pressure tap on the stator disk
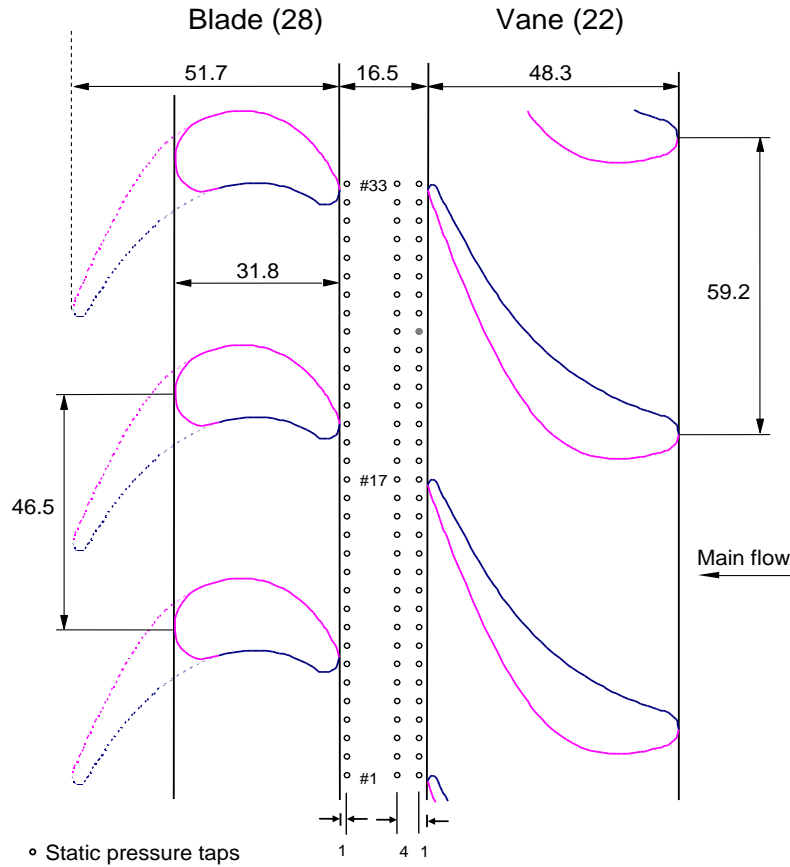
Fig. 2.7 Static pressure taps on the outer shroud

Pressure tap locations

Pressure taps were provided in the disk cavity as well as in the main gas path. In the cavity, the taps were on the stator disk surface along a radial line at eight locations (r = 45 mm, 81 mm, 104 mm, 123 mm, 148 mm, 162 mm, 173 mm and 187 mm); of these, four locations were in the inner cavity and the remaining four in the rim cavity, Fig. 2.3. Additionally, six pressure taps were provided circumferentially over one vane pitch at r = 173 mm and 17 pressure taps at r = 187 mm to measure the circumferential variation of static pressure in the rim cavity. The static pressure distribution on the stator rim seal (or vane platform)

17

was to be measured at 1 mm downstream of the vane trailing edge plane via 17 pressure taps distributed over one vane pitch. In the main gas path between the vane trailing edge and the blade leading edge, 33 pressure taps were provided over two vane pitches circumferentially at each of three axial locations (1 mm, 5mm and 15.5 mm downstream of the vane trailing edge), as shown in Fig. 2.7.

Scanivalve

      Scanivalve (48J9-2621) is an oil-less pressure sampling scanner used for measuring multiple pressures. It has 48 inlet channels connected to the turbine rig pressure taps by flexible vinyl tubes (VINL-063, Scanivalve Corp.) and one outlet channel connected to the pressure transducer. A solenoid-controlled stepper drive operated manually rotates the 48-channel fluid switch wafer such that only one of the 48 inlet channels is connected at a time to the outlet channel. The particular inlet channel connected to the outlet channel is identified by a position encoder/decoder who transmits the angular position of the Scanivalve to a display unit.

Pressure Transducer

      A variable-reluctance type differential pressure transducer (DP45-32, Validyne) with a range of 0 - 2 psi (0 - 14kPa) was used to measure the static gage pressure. The transducer has a magnetically permeable diaphragm clamped between two blocks of stainless steel, each embedded with an inductance coil. The diaphragm is provided with a pressure port on its either side with one port kept open to the ambient and the other connected to the output from the Scanivalve. The deflection of the diaphragm toward the low pressure side changes

the inductance in each coil and produces an output voltage proportional to applied pressure difference.

Pressure Signal Carrier Demodulator

A high-gain pressure carrier signal demodulator (CD12-A-1-B, Validyne) was employed to provide transducer excitation as well as to amplify and demodulate the output of the variable-reluctance type pressure transducer. The input range of the carrier demodulator is selected by a three-position switch which can be set at 1, 3, and 15 mV/V. It has a high input sensitivity range (0.9 to 75mV/V) which allowed sensing of small fluctuations in the input signal. The CD12 analog output is displayed on the front panel as well as routed to a data acquisition system.

Data Acquisition System

Analog output from the carrier demodulator was further processed by a Universal Waveform Analyzer (Analogic, DATA 6500). The Analyzer was programmed to provide the time-mean and RMS of the pressure signal over a sequence of 30720 data points with a sampling period of 500 µs.

2.2.2   Experimental Procedure

After the rig attained the required nominal steady state condition as defined by the main air flow rate, rotor speed, and secondary (purge) air flow rate, static gage pressures were measured at the different pressure tap locations. As discussed earlier, the Scanivalve was used to sequentially connect the pressure taps to the differential pressure transducer. The analog signal from the CD12 was

19

routed to the data acquisition system which displayed the mean and RMS values of the measured gage pressure.

The time-average static gage pressure is defined as

$$\bar{p} = \frac{1}{T} \int_0^T p(t)dt \approx \frac{1}{N} \sum_{i=1}^N p_i \qquad (2.1)$$

In order to average out the pressure fluctuations arising from blade passage, the sampling rate of the data acquisition system was kept sufficiently high. The data acquisition system was set to acquire 30720 data points (N) at 2 kHz (500 μs sampling interval); the lowest and the highest blade passage frequency for the experiments were, respectively, 0.887 kHz (for 1900 rpm rotor speed) and 1.12 kHz (for 2400 rpm rotor speed).

The main and purge air inlet pressures were measured, respectively at, the outer shroud 20 mm upstream of the vane leading edge plane and at the purge air supply tube wall 70 mm upstream of the disk cavity entrance. The exit static pressure of the main air mixed with the purge air was measured on the steel outer shroud 24 mm downstream of the blade trailing edge plane. These three pressures prescribe the entrance and the exit pressure conditions for the turbine stage.

2.3   Disk Rim Cavity Velocity Field Measurement

To investigate the velocity field inside the rim cavity, the Particle Image Velocimetry (PIV) technique was used. In this non-intrusive method, instantaneous maps of velocity vectors are obtained by measuring over a known time interval, the displacements of small seed particles (1-2 μm dia.) which accurately follow the motion of the surrounding fluid.

2.3.1 Principle of PIV

The fluid whose motion is to be mapped is uniformly seeded with fine light-scattering particles. In two-dimensional PIV, the plane of interest is illuminated by two laser light pulses separated by a very short and precisely known time interval. A high-speed digital camera, equipped with a CCD sensor, records the light scattered by the particles in two different frames - one for each light pulse. The camera output is stored in the memory of a computer.

The local displacement of the seed particles is then statistically estimated from this image pair by dividing them into subareas called 'interrogation spots'. Each interrogation spot from the first image is cross-correlated with the corresponding interrogation spot from the second image. The highest peak in the cross-correlation gives the mean displacement vector for that interrogation spot. The local velocity vector in the plane of measurement is then calculated by taking into account the time gap between the two images and the image magnification. Similar examination of all other interrogation spots yields the velocity field in the plane of the laser sheet.

2.3.2 System Components and Parameters

Figure 2.8 shows the set-up for PIV experiments. The PIV system components are listed in Table 2.1 and their description follows.

Table 2.1 PIV – system components

Component	Component description
Seed particle generation	Laskin nozzle particle generator (1-2 μm dia. olive oil particles)
Light sheet optics	- 40 mm cylindrical lens; 1000 mm spherical lens
Recording device	Power View 4M CCD camera (TSI)

External trigger	He-Ne laser, photoelectric detector/ amplifier (TTL signal)
Synchronizer	Model 610034, TSI
Image acquisition and processing	Insight 6.1 software

Seed particle generation and supply

In PIV, the velocity of the flow is indirectly determined from the velocity of the tracer (seed) particles. Hence, it is imperative for the particles to follow the flow faithfully. In the moving fluid, the particles are subjected to drag forces linearly proportional to their size. As such, it is important to have particles of sufficiently small diameter (assuming spherical seed particles). The particles also need to scatter enough light to be detected by the camera, the intensity of scattered light being linearly proportional to the particle diameter. Due to the two contradictory requirements of the particle diameter, a tradeoff is necessary.

For our PIV experiments, a Laskin nozzle particle generator was used to generate 1-2 µm diameter olive oil droplets ($\approx$ 1.5 µm mean diameter). Compressed air of 4 to 5 psig pressure was used to atomize the olive oil and provide high enough particle concentration for reliable velocity measurements. The seed particles were introduced into the purge air flow approximately 1.8 m upstream of its entrance to the disk cavity.

Light source

Laser light is the preferred light source for PIV experiments because of their high energy density, monochromatic nature and ease of forming thin light sheet.

Fig. 2.8 The particle image velocimetry setup

N₂ cylinder

PIV 200 laser

Laser power

Counterweight

Beam launching mount

Synchronizer

Laser arm

Traverse + Optics

Computer with frame-grabber

Rotor

Light sheet

INSIGHT6.1

Fibre optic cable

Plexiglass stator

He-Ne laser

Signal generator

Powerview camera + traverse
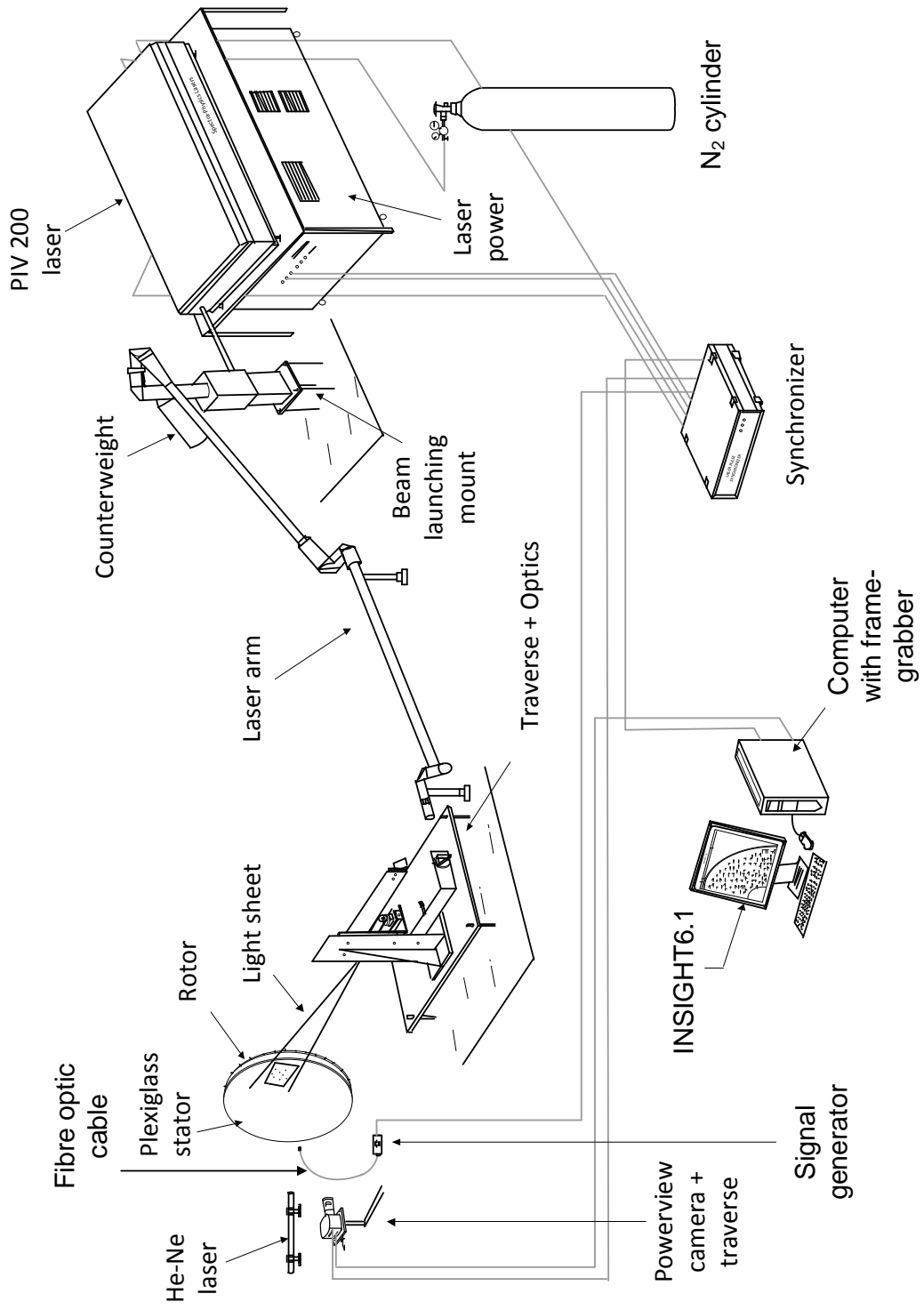
For the experiments conducted, a dual-cavity Nd:YAG laser (Spectra-Physics GCR-200) was used. Inside the laser, high-intensity flash lamps were utilized to achieve excitation of the lasing medium. A Quality switch (Q-switch) was used which, when operated at the point of maximum population inversion causes high cavity loss and results in a short pulse with high peak power. Short pulse prevents streaking of particles in the images and high power of the laser light helps in good scattering of the light. An optimum Q-switch delay of 165 μs was used in the experiments. The laser produced pulses of 10 ns width with an output energy of 200 mJ per pulse at a maximum repetition frequency of 10 Hz. The average power of the two laser pulses was 2.0 W and the peak instantaneous power was 20 MW. It is important to have equal power in both the laser pulses to get identical illumination of the same particle in the two images and this was ensured by using a power meter.

The laser also employed KD*P crystals, which functioned as a harmonic generator, to convert infrared light of 1064 nm wavelength to green visible light with wavelength of 532 nm. The short wavelength leads to thinner light sheets and improved particle light scattering.

Light sheet optics

The 9 mm diameter beam from the laser was directed to the light sheet optics system comprised of spherical lens-cylindrical lens combination. The beam diameter and the field of view (FOV) to be illuminated determine the lens combination to be used. As seen in the Fig. 2.9, the focal length of the cylindrical lens governs the light sheet height and the focal length of the spherical lens
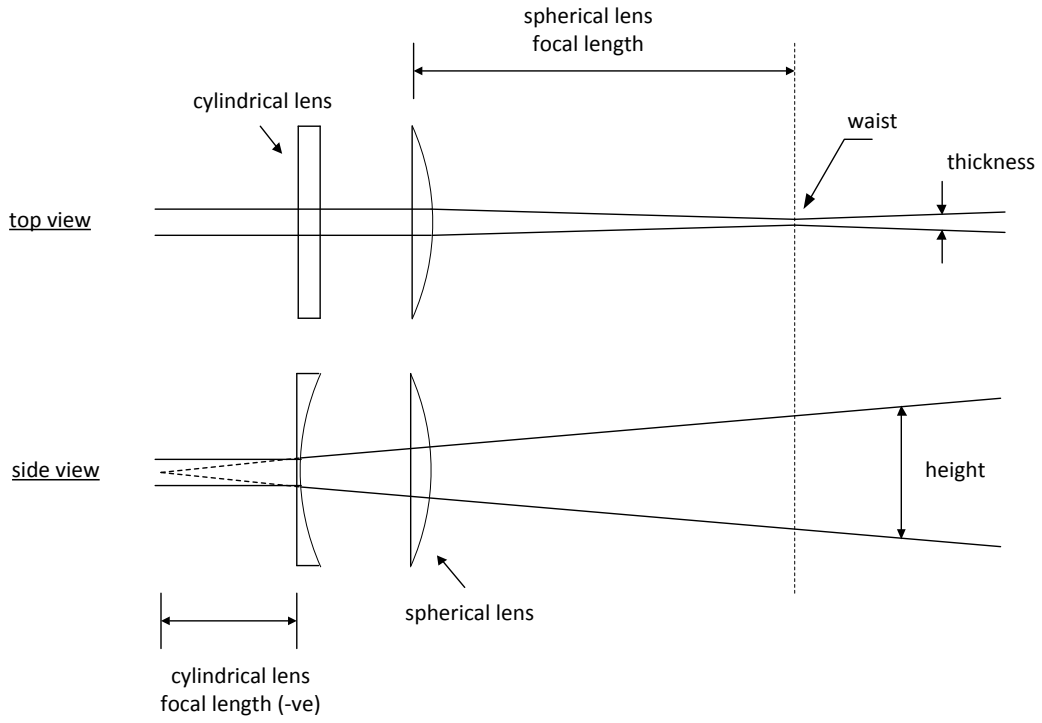
Fig. 2.9 Light sheet optics
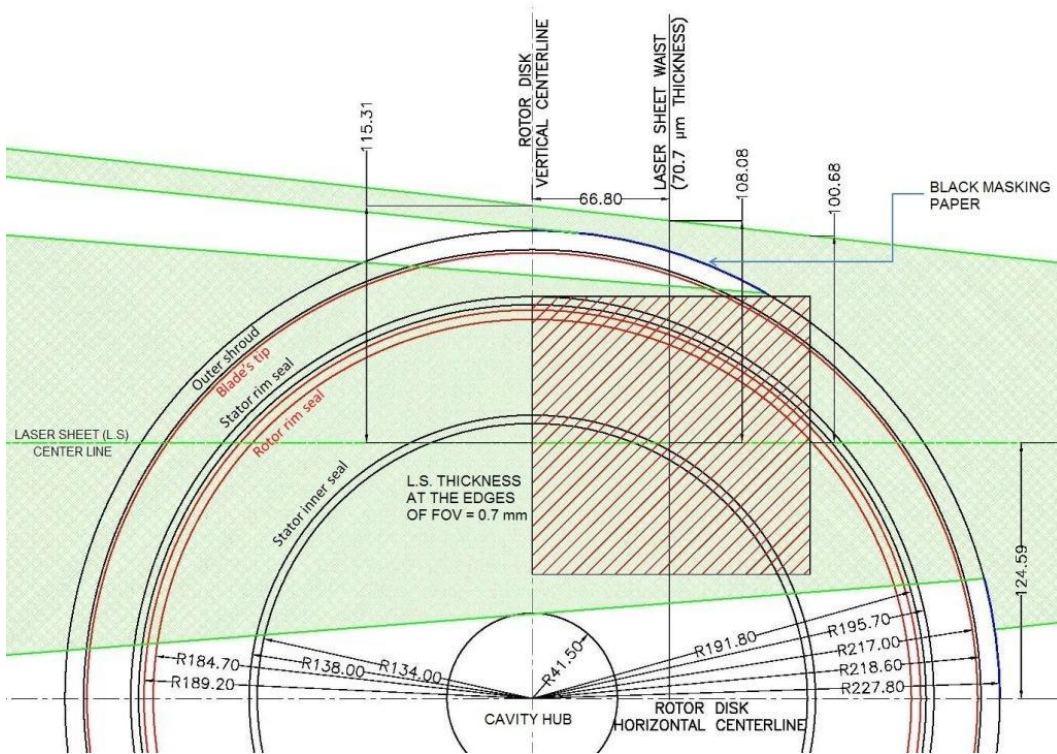
Fig. 2.10 PIV - Field of view

governs its thickness. It should be noted that increasing the light sheet height decreases its intensity. For the present experiments, a cylindrical lens of focal length - 40 mm and a spherical lens of focal length 1000 mm were selected. The light sheet height at the near end of the FOV was 201 mm and at the far end of the FOV 231 mm, Fig. 2.10. At the waist, the height was 216 mm. The light sheet thickness was 700 µm at the near and far edges of the FOV while at the waist it was only 70.7 µm.

The light sheet was positioned in the rim cavity with the help of a three-dimensional traverse on which the light sheet optics system containing two right-angled prisms (BK7) and the lenses was mounted. The lenses were mounted on a horizontal rotary base to render the light sheet parallel to the rotor surface. The laser beam was directed from the laser to the optics by an adjustable light arm. The light arm consisted of a counterweight and a series of rotating knuckles, specially coated mirrors, and aluminum tubes forming a fully enclosed device.

Digital image recording

The PIV images were obtained using a high speed digital Cross-Correlation camera (Power View 4M, TSI). The camera had a charge-coupled device (CCD) sensor which contained 2048 x 2048 light-sensitive pixels, each of 7.4 µm x 7.4 µm size, arranged in a square array. When light photons impinge on the light sensitive area, an electrical charge is produced. The generated charge is proportional to the number of photons that hit the sensor. An analog-to-digital convertor then reads the charge value of each pixel and converts it into a digital value.
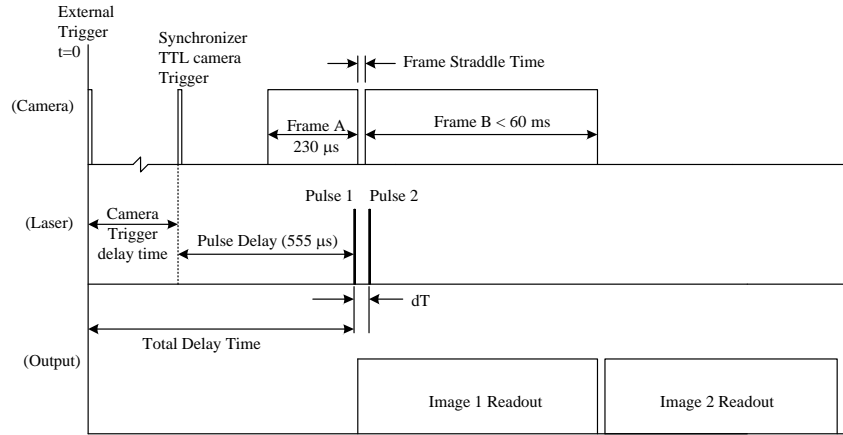
Fig. 2.11 Camera timing diagram

The double-frame/single exposure technique of the present work allows capturing of the two images on two different frames, 'frame straddling', Fig. 2.11. This removes the directional ambiguity while cross-correlating the frames, and also improves the dynamic range for velocity. When measuring velocities of a few meters per second the time interval between the two laser pulses, δT, is restricted to a few mirco-seconds. But, the time required to transfer an image directly from the camera CCD to a computer is much larger. Hence, to enable frame-straddling, the camera used in the experiments featured a special progressive scan interline transfer CCD array. In this CCD array, each active pixel has a masked charge storage area next to it which allows the charges acquired by the pixels in the first image (frame A) to be transferred to the adjacent memory dump rapidly (in the order of nano-seconds). This permits full electronic shuttering of the entire first image between the laser pulses and help reset the active pixels for the second image (frame B). The accumulated charge in the memory storage from frame A is transferred sequentially (progressive scan) one

27

row at a time into an analog shift register and then read out by a charge-to-voltage converter. This data is then transferred to the *frame grabber* installed in the computer via an LVDS cable. Meanwhile, the active pixels hold on to the charges from the second frame. After the first image read-out is over, the second image is transferred to the computer in a similar manner. Thus, both the second image acquisition and the first image read-out take place in parallel; this facilitates frame-straddling. Figure 2.11 shows the timing diagram for the camera.

Due to the presence of the masked area, the available light sensitive area of the CCD array is reduced. Hence, micro-lenses are deposited on the pixel array to enhance the collection of incoming light. The fill ratio, which is the measure of the percentage of available light sensitive area in a CCD array, is 60% (with micro-lenses) for the camera used.

For the given frame rate of the camera (8.5 Hz or 4.5 Hz frame pair rate), PCI bus limit of the frame grabber (120 MB/sec), operating frequencies of the laser (10 Hz, 5 Hz, 3.33 Hz), size of each image (8 MB) and the computer memory (2 GB), the maximum frame pair-rate for the system was 3.33 image per second.

Image synchronization

In order to acquire two good correlatable images, it is critical to synchronize the working of all the components. For the PIV experiments, the timing and the sequencing of the events was software-controlled by INSIGHT 6.1 via a synchronizer (Model 610034, TSI). The synchronizer was connected to the laser, external trigger, camera and computer.

The images were acquired at the same vane and blade positions for all experiments by triggering the synchronizer using a TTL (Transistor-Transistor Logic) signal generated once every rotor revolution. An aluminum strip, 2 mm wide and 12 mm long and radially aligned with a rotor blade tip, reflected light from a low power He-Ne laser (7 mW, Melles Griot). This reflected light was received by a photoelectric detector/amplifier via a liquid light guide (Newport Corporation, Oriel Light sources, VIS liquid light guides, Model 77569). The photoelectric detector/amplifier converted the light signal into a +4.5 V square pulse, which is the TTL high required to trigger the synchronizer.

Immediately after the synchronizer receives the trigger signal, it begins the image capture and laser pulsing sequence, Fig. 2.11. The time from the start of the sequence (t=0) until the camera is triggered by the synchronizer is known as the "camera trigger delay time". This parameter is adjusted so as to make measurements at a specific position of the rotor. The first frame is of very short duration, 230 μs. The time from the start of the camera trigger until the first laser pulse is the "pulse delay time"; this is adjusted so as to pulse the first laser exactly at the very end of the first frame. The Nd:YAG laser requires two signals (these are provided by the synchronizer) to create a laser pulse; one for the flashlamp and the second to open the Q-switch that pulses the laser. The time from the end of first frame to the start of the second is called as the "frame straddle time". Within this short period of time, the frame A data is transferred to the adjacent storage sites and the CCD array is reset to capture the second image. The frame B exposure time is kept long enough to let the camera transmit the first image data

through to the *frame grabber* before the second image data moves into the readout registers. The synchronizer ignores the external trigger until the entire pulse sequence is completed.

2.3.3   Experimental Procedure and Processing

Image acquisition

PIV maps of velocity field in the radial-azimuthal plane were acquired at four axial positions in the rim cavity. The laser light sheet was introduced into the cavity through the polished plexiglass outer shroud. Two axial locations were near the stator, 1.9 mm and 2.6 mm from the stator surface; and two axial locations were near the rotor, 2.6 mm and 4 mm from the rotor surface, Fig. 2.12. It was not possible to obtain maps in planes midway through the cavity because of scattering and attendant reduction in the laser light intensity when passing through the two axially overlapping rim seals.

The cross-correlation camera was mounted on a three-dimensional traverse that allowed it to be positioned to the mapping area of interest and the magnification required. A 50 mm camera lens (Nikon Micro-Nikkor) with an f-ratio of 2.8 was used in all the experiments.

The image magnification factor of 0.1075 for the setup was manually obtained with the help of a quarter sector graph sheet, taped flat onto the rotor surface. The two right-angled edges of the graph sheet were made exactly horizontal and vertical using the continuous mode of the camera in the INSIGHT software. The camera was focused sharply on the graph sheet and the x and y pixel differences between two points, a certain known x and y distance apart,

were calculated. From this, and the fact that each pixel was a square of side 7.4 μm, the image magnification was obtained. The magnification value was verified at other random locations. From the magnification and the active area of the CCD array (15.2 mm x 15.2 mm), the field of view was calculated to be 141.308 mm x 141.308 mm.

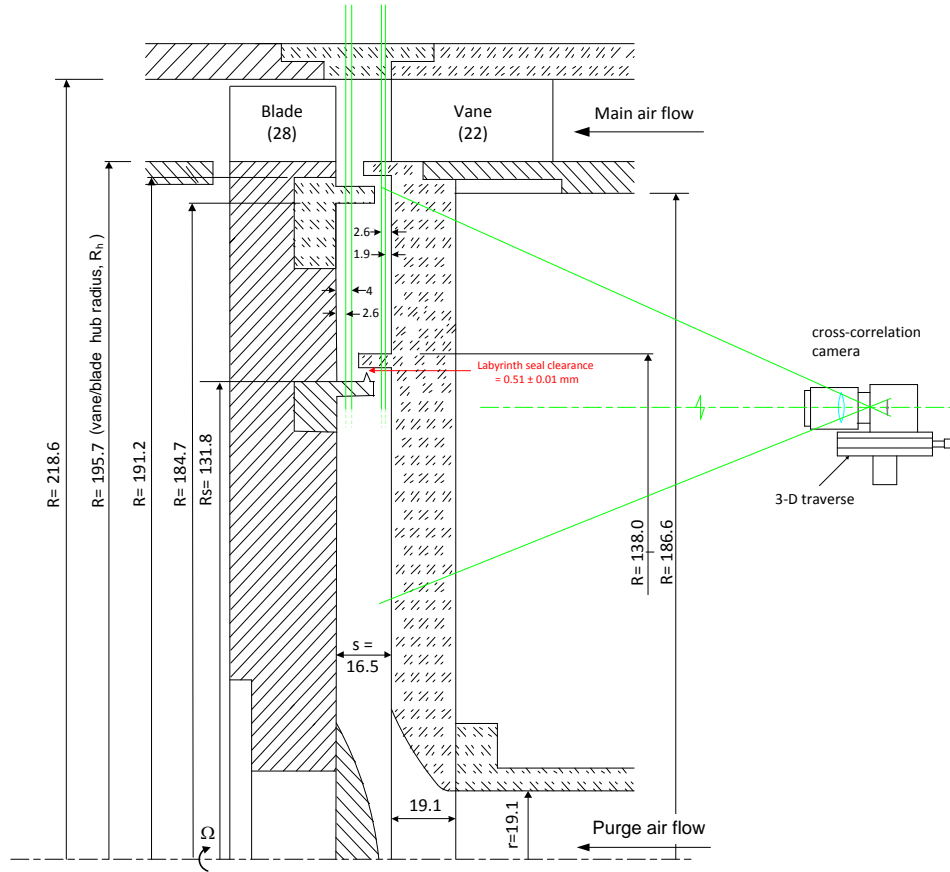Fig. 2.12 Laser light sheet axial positions in the disk cavity, all dimensions in mm.

Figure 2.13 shows the quadrant of the rim cavity that was imaged. The mapped region extended from a radius of 138 mm (outer radius of the labyrinth seal) to a radius of 189.2 mm (outer radius of rotor rim seal) for the 'near stator' axial positions and to a radius of 184.7 mm (inner radius of rotor rim seal) for the

31

'near rotor' axial positions. These radii are denoted by the dashed circular arcs. The vane (V) and blade (B) locations at the instant of image capture are also shown. At the maximum rotor speed of 2400 rpm, the blade positions shift azimuthally by less than 0.3° during a pulse separation time of 15 μs. Ten instantaneous maps were obtained at each position to allow ensemble-averaging when necessary.

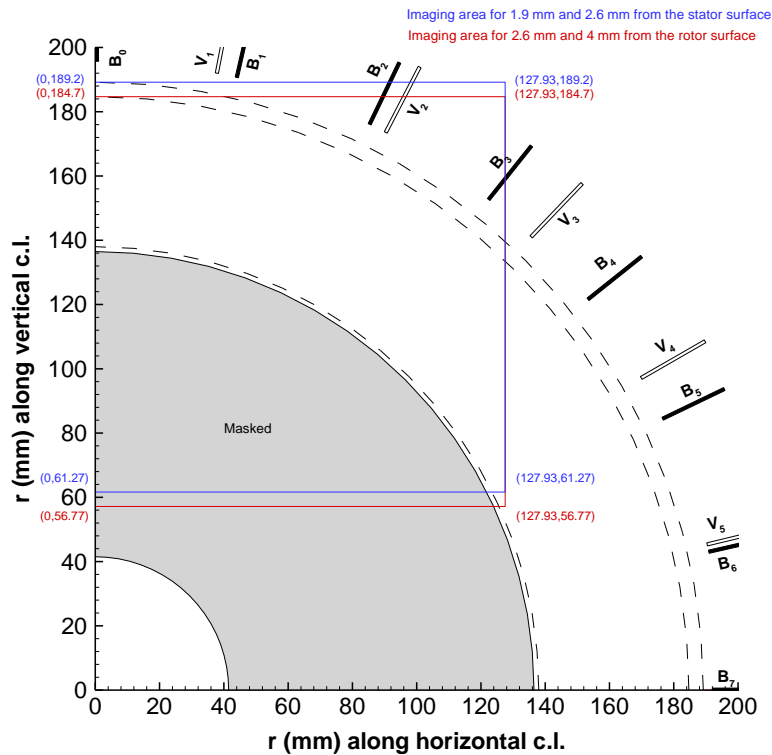Fig. 2.13 The mapped quadrant of the disk cavity showing vane/blade positions at the instant of image capture

The INSIGHT 6.1 (TSI Inc.) software automates the process of image acquisition, analysis and validation. It acts as a control module to coordinate the process of image capture with the synchronizer. The software allows the user to set parameters such as pulse pair repetition rate (Hz), pulse delay time (ms),

camera trigger delay time (ms), Q-switch delay time (μs), and pulse separation time, δT (μs). δT was chosen to be 15 μs for $c_w = 1540$, and 12 μs for $c_w = 3080$ and 4621. This was to accommodate the faster out-of-image plane particle motion at higher secondary flows.

Processing

Each of the acquired image pairs was processed using the INSIGHT software to extract the velocity vector field. The steps involved in this processing are: image conditioning, grid generation, spot masking, correlation, peak location and vector validation. These steps are shown in a flow chart in Fig. 2.14.

Background Subtraction Image Processor

Before beginning PIV processing, an optional step of eliminating background noise, image conditioning, may be applied to the acquired images. This step is particularly helpful for PIV experiments near the rotor where, due to the depth of field of the camera, the light reflected from the rotor surface is also seen in the images. Processing of such images tend to show rotor surface velocities in the image. To remove them, a set of 5 image pairs were obtained before the introduction of the olive oil particles. These background images were then processed using the *Average Intensity Image Processor* which finds over the sequence of images and over each pixel, the average intensity of those pixels. This average image pair was then subtracted from the raw images obtained in the actual experiment, prior to their processing.
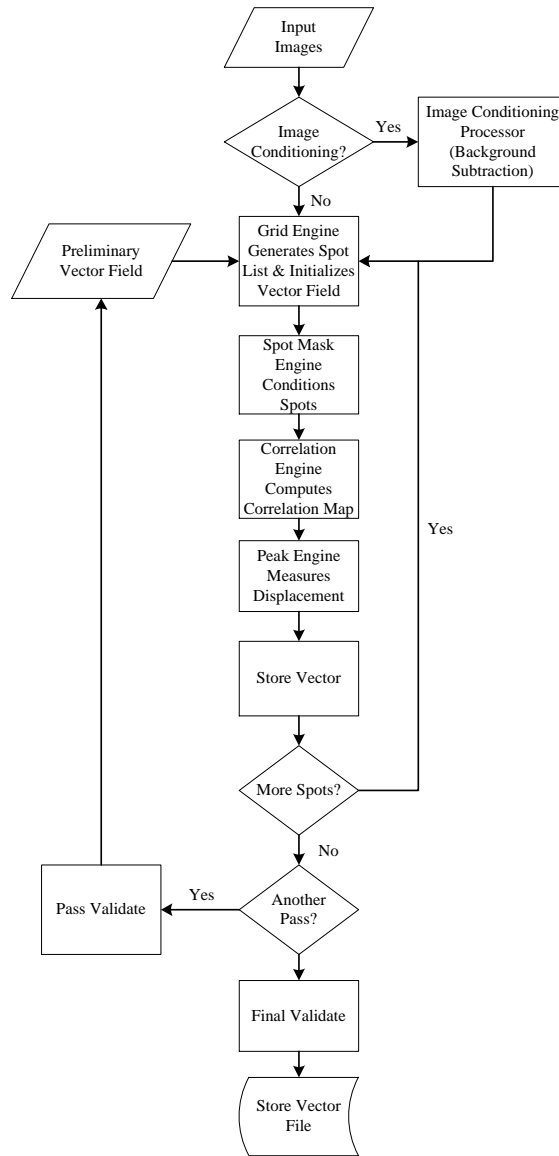
Fig. 2.14 Flow chart of image processing steps in INSIGHT 6.1

Grid Engine

The function of the grid engine is to break up the image frames into smaller spots. Spot 'A' and Spot 'B' refer to the spot sizes, in pixels, for frame A and frame B respectively. The 'RecursiveNyquistGrid' was used for increased accuracy and higher spatial resolution. This grid engine processes the images in

multiple passes. The first pass computes the vector field at the starting spot sizes with 50% overlap grid spacing with no spot offsets. The result of the first pass are used to optimize the spot offsets for the second processing pass so that it will have a peak location within half a pixel of the correlation center. If the final spot size (used for the second pass) is half of the start spot size (used for the first pass), then four times the initial number of vectors will be obtained. If the starting and final spot sizes are kept the same, the second pass uses the optimized window offsets to recompute the vector field with the same number of vectors.

For the conducted experiments, a start spot size and a final spot size of '32 x 32' pixels for both Spots A and B was found to give a good velocity distribution.

Spot Mask Engine

Spot mask engine is used to modify or condition the image spots before they are processed. Certain correlation engines (such as FFT correlator) can work with only square spot sizes. The spot mask engine pads the non-square spots with zero intensity pixels to convert them into square spots. Since the selected correlation engine, Hart Correlator, can work with non-square spots, the 'No Mask' spot mask engine was used.

Correlation Engine

The correlation engine computes the correlation function of the spots A and B returning the results as a correlation map. The correlation function is an algorithm which numerically calculates the correlation of the spot intensity at all pixel displacements within the allowed displacement range. The highest

correlation map pixel is assumed to be the particle image displacement peak caused by the contributions of many particle pairs.

The 'Hart Correlator' correlation engine was selected for our experiments since it reduces sub-pixel bias errors and eliminates spurious vectors from the velocity vector field. It is a direct correlation method that processes only the most significant pixels to improve processing speed. The compression ratio is used to set how many pixels are used in computing the correlation. A high compression ratio increases the processing speed. A lower value will include more pixels in the correlation which may, or may not, improve the correlation map signal-to-noise ratio. The default compression ratio value of 0.9 was used in the experiments implying that 10% of the most significant spot pixels were used in computing the correlation, while the remaining 90% of the pixels were excluded.

A maximum displacement of 8 pixels was used to limit the correlation map search area from the zeroth pixel to increase processing speed and decrease memory use.

The peak engine analyzes the correlation map created by the correlation engine and determines the location of the particle image displacement peak. When the 'Hart Correlator' is selected, 'Bilinear Peak' is set as the default peak engine.

Errors in PIV image processing can occur due to out-of-plane particle motion, low seed particle density or from errors in correlation, resulting in spurious vectors. To eliminate them, the INSIGHT software provides various inbuilt validation filters such as standard deviation, range, median, mean and smooth.

Post Processing

The vector file generated by the INSIGHT software contained the u(x) and v(y) velocity components, in pixels, at the corresponding pixel co-ordinates. Making use of the camera magnification value, δT, and the FOV position in the disk cavity, a MATLAB program was used to convert the pixel velocities to real co-ordinates. The radial and tangential velocity components were also calculated for each velocity vector location. The MATLAB generated data file was then plotted in TECPLOT FOCUS 2010 to show the velocity vector map.

Chapter 3

RESULTS AND DISCUSSION

3.1   Experimental Conditions

In order to understand the fluid flow field in the rim cavity, experiments were conducted for two different sets of rotor speeds and mainstream gas flow rates, and several different purge air flow rates as shown in Table 3.1. In the table, the experimental conditions are specified using non-dimensional parameters: main gas flow Reynolds number (Re_{vax}), rotor disk rotational Reynolds number (Re_{ϕ}), and non dimensional mass flow rate of purge air (c_w).

Table 3.1 Experimental conditions

Expt. Set No.	Mainstream Gas Flow Rate (Re_{vax})	Rotor Disk Speed (Re_{ϕ})	β_2 (°)	Free Disk Pumping Flow Rate ($c_{w,fd}$)	Purge Air Flow Rate (c_w)
I	9.27×10^4	4.85×10^5	49.7	7745	770
					1540
					3080
					4621
					6161
II	1.12×10^5	6.14×10^5	48.3	9354	770
					1540
					3080
					4621
					6161

The rotor speeds and main air flow rates were selected such that the angle β_2 was maintained at a large positive value which ensured that the rotor operated in the turbine mode. The shape of the velocity triangle downstream of the vane trailing edge was conserved for the two sets of experiments. This was because, according to Roy et. al. (2005), the velocity triangle affects the ingestion process.

The purge air flow rates were chosen with reference to the free disk pumping flow rate ($c_{w,fd}$), this being the pumping flow rate due to a flat disk rotating in a quiescent environment.

The time-average static pressure measurements were carried out initially for all the experimental conditions of Table 3.1. Tracer gas concentration measurement experiments were also conducted, details of which can be found in Thiagarajan, 2013. PIV experiments were performed for the two experiment sets but for $c_w = 1540$, 3080 and 4621 only. At $c_w = 770$ the purge air flow rate was too low to obtain a good seed particle density, while at $c_w = 6161$ the cavity flow was not expected to be very different from at $c_w = 4621$.

For all of the experiments, the average laboratory ambient temperature was 23°C and the average laboratory ambient pressure was 101.375 kPa.

Time-Average Static Pressure Distribution

The time-average static pressure distributions in the main gas annulus flow were obtained over two vane pitches at three axial locations on the outer shroud and over one vane pitch at one axial location on the vane platform. Measurements were obtained in the disk cavity at eight radial positions on the stator disk surface. The pressure tap locations are as shown in Figs. 2.3 and 2.7.

Figure 3.1 shows the circumferential distribution of time-average static pressure on the outer shroud and the vane platform for experimental set II, $c_w =$ 1540. These measurements demonstrate that nominally steady, circumferentially periodic flow was achieved in the main gas path with the periodicity following the vane pitch. The pressure asymmetry produced by the vanes is maximum just
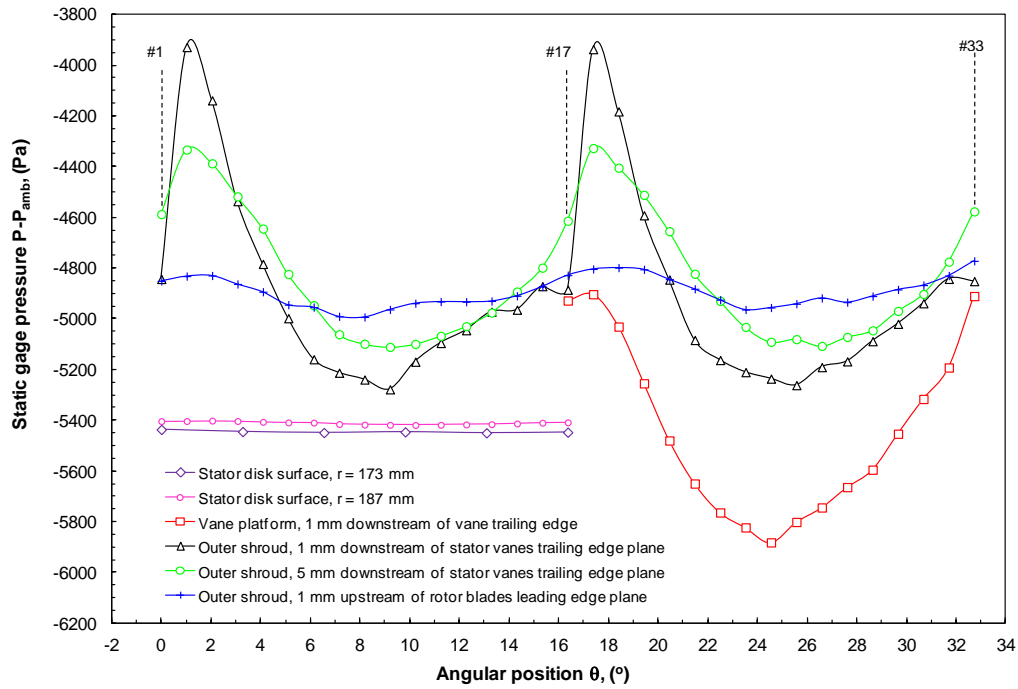
Fig. 3.1 Circumferential distribution of time-average static pressure at the outer shroud, vane platform, and stator disk near its rim – $Re_{vax} = 1.12 \times 10^5$, $Re_\phi = 6.14 \times 10^5$, $c_w = 1540$
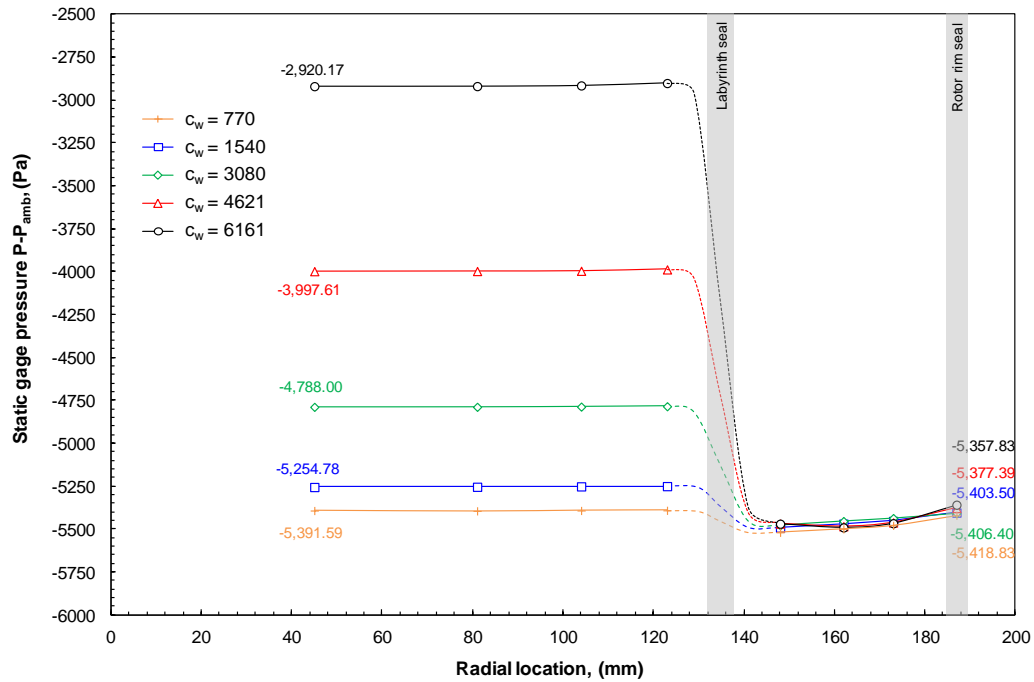

Fig. 3.2 Effect of c_w on the radial distribution of time average static pressure in the disk cavity at the stator disk for $Re_{vax} = 1.12 \times 10^5$, $Re_\phi = 6.14 \times 10^5$

40

downstream of the vane trailing edge, its strength decaying gradually towards the blades.

The pressure on the vane platform and in the rim cavity on the stator surface is considerably lower than at the outer shroud. Circumferential variation of pressure is not discernible on the stator disk surface even near its rim (r = 187 mm) which indicates that the pressure asymmetry in the mainstream flow due to the vanes is dissipated across the rim seals. The differential between the main gas flow pressure near the stator rim seal edge and the rim cavity pressure near the seals could cause the ingestion of main gas into the cavity.

Figure 3.2 shows the radial distribution of pressure at the stator disk surface for experiment set II. As c_w increases, the inner cavity pressure level increases markedly. This built-up pressure is seen to drop across the labyrinth seal to a small range of low pressures for all purge air flow rates.

An increase in the purge air flow rate decreases the average pressure level in the main gas path and marginally increases the pressure near the cavity rim. This effectively reduces the potential for main gas ingestion.

## 3.2   Velocity Field in the Disk Rim Cavity

PIV maps were obtained at four axial positions inside the rim cavity at varying purge air flow rates. Two axial positions near the stator surface (1.9 mm and 2.6 mm from the stator) and two axial positions near the rotor surface (4 mm and 2.6 mm from the rotor) were chosen. Ten instantaneous vector maps were obtained at each position. It should be noted that even though the vane-blade positions remained identical for each map, the velocity vector field near the rim

seals did not repeat in all the ten vector maps. Ensemble-averaging of the ten maps offered a smoother picture of the fluid velocity in the vicinity of the rim seals. For each experiment, one representative instantaneous vector map was chosen from the ten and analyzed. For brevity, only results for experiment set II 1.9 mm from the stator surface and 2.6 mm from the rotor surface are discussed in detail. Results for the other two locations are similar to their respective closest positions; the significant differences between them are discussed later.

<u>Case of $Re_{vax} = 1.12{\times}10^5$, $Re_{\phi} = 6.14{\times}10^5$, $c_w = 1540$</u>

Figure 3.3(a) shows, for this experimental condition, an r-ϕ plane instantaneous velocity vector map at 1.9 mm from the stator surface in one quadrant of the rim cavity. The two dashed lines at the outer periphery represent the rotor rim seal location and the dashed line radially inboard represents the labyrinth seal outer edge. Also shown are the azimuthal positions of the vanes (V) and the blades (B) at the time instant of image capture. It is important to note these, since the relative positions of the vanes and blades and their associated pressure fields are known to influence the velocity field and the associated ingestion process. The map shows circumferential bands of increasing velocity along the radius. Since the flow is tangentially dominated at the low purge air flow rate, it is hard to visualize the radial component of the velocity, especially near the rim seals. Figure 3.3(b) shows the vector map of the radial velocity component for the same instantaneous file. Near the rim seal, non-periodic regions of outward and inward radial vectors can be seen. Two sectors of 3° each, one with maximum inward velocities near the rotor rim seal (bracketed by the two

42
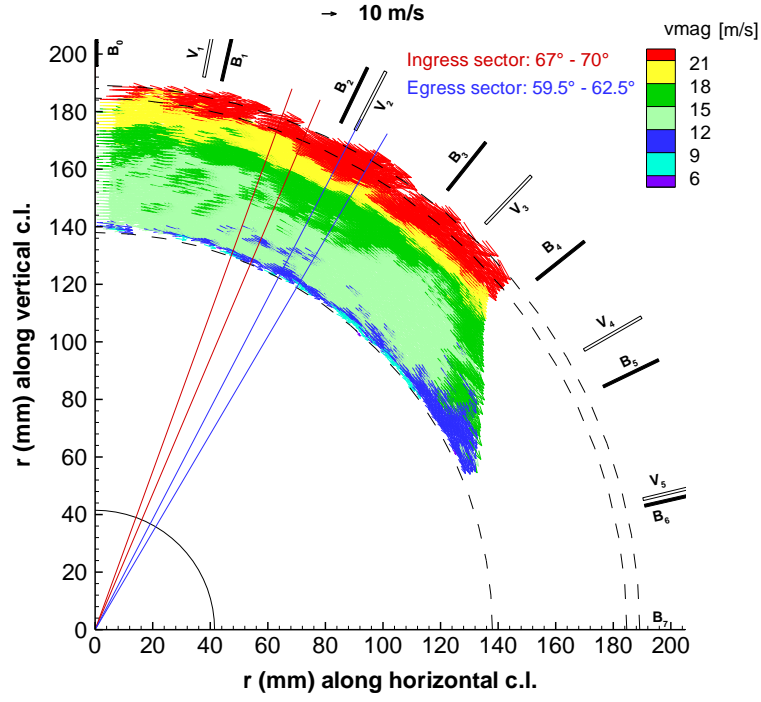
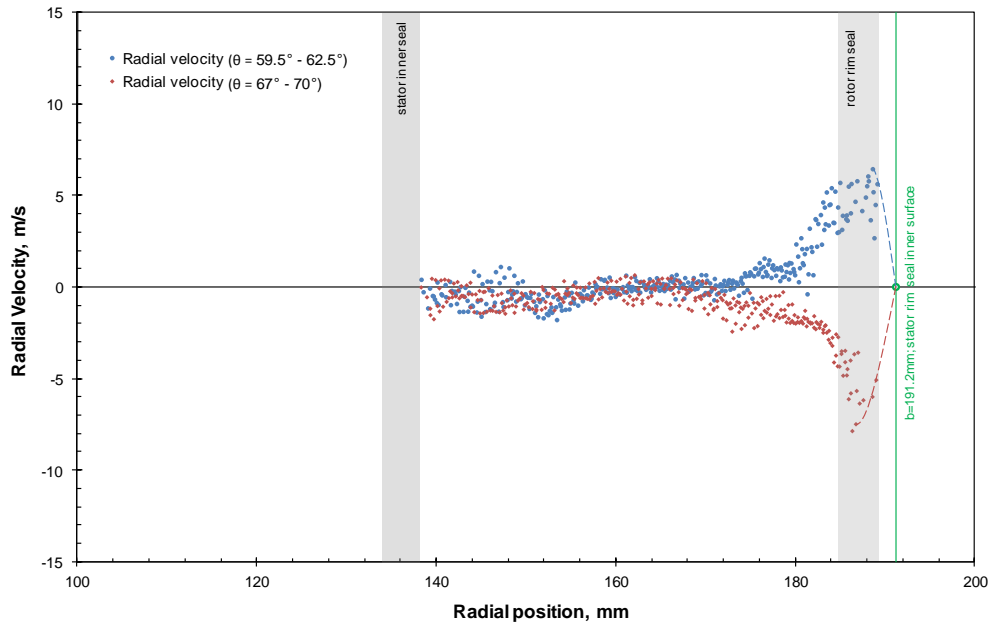(a)   Instantaneous velocity
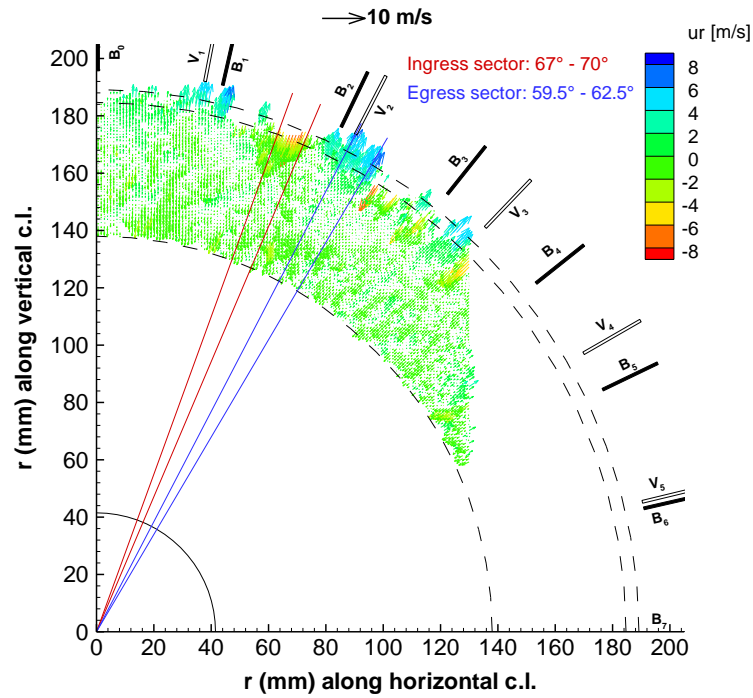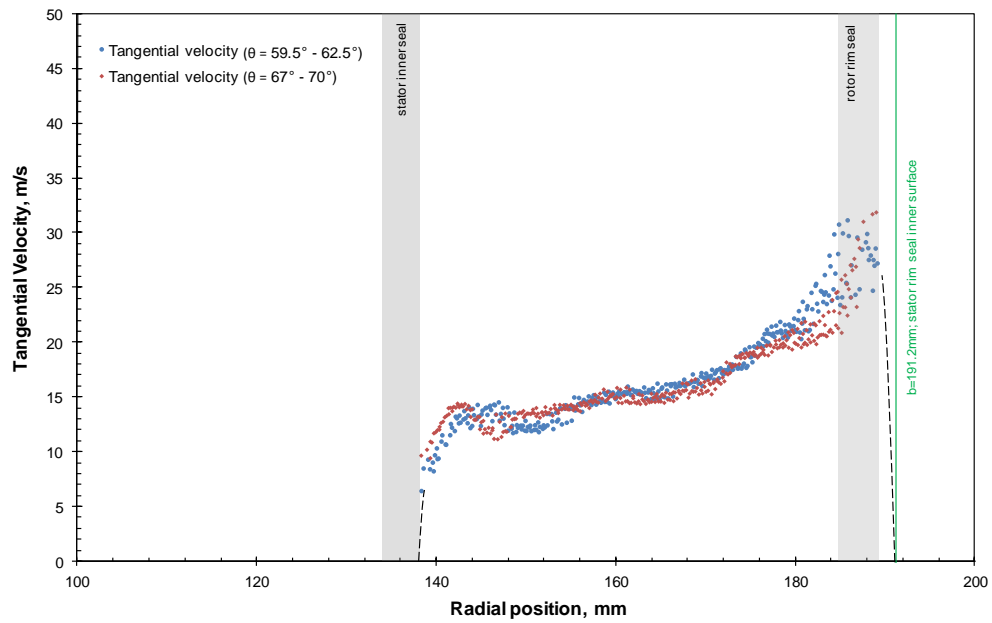

(b)   Instantaneous radial velocity

Fig. 3.3 r-ϕ plane instantaneous velocity vector maps in the rim cavity at 1.9 mm from the stator surface – $Re_{vax} = 1.12 \times 10^5$, $Re_\phi = 6.14 \times 10^5$, $c_w = 1540$ ($\delta t = 15$ μs)
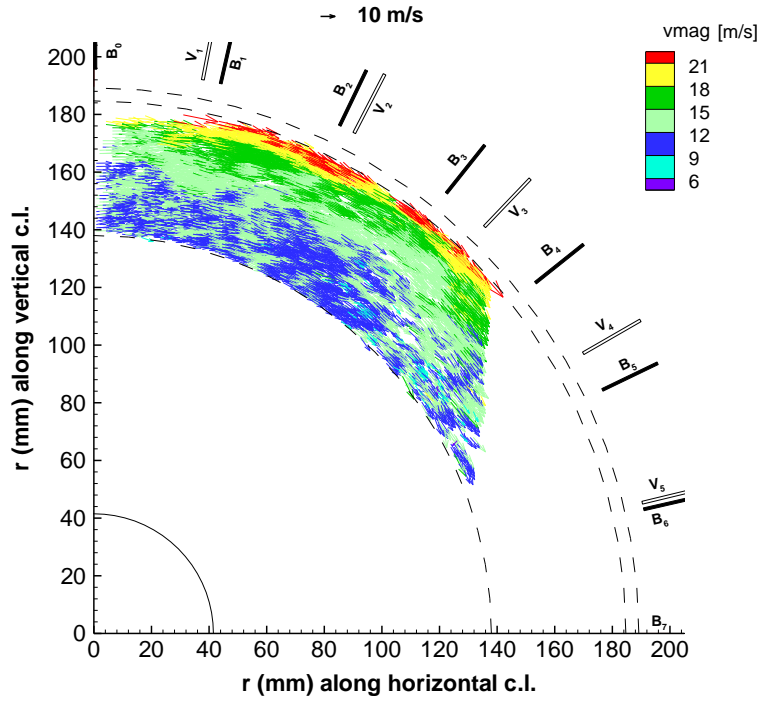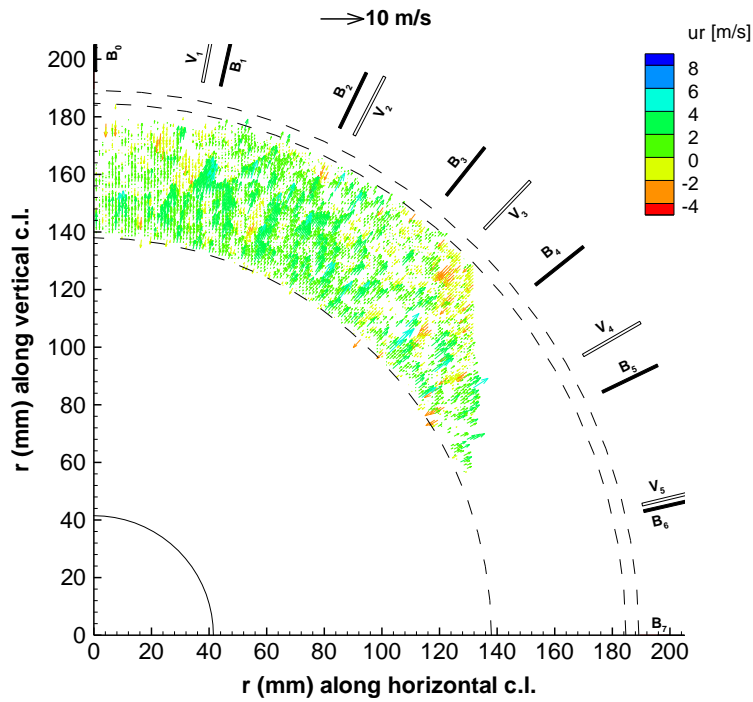
43

(a)   Radial Velocity

(b)   Tangential Velocity

Fig. 3.4   r-ϕ plane instantaneous radial and tangential velocities in the rim cavity at 1.9 mm from the stator surface − $Re_{vax} = 1.12 \times 10^{5}$, $Re_{\phi} = 6.14 \times 10^{5}$, $c_{w} = 1540$ ($\delta t = 15$ μs)

red lines) and another showing maximum outward velocities near the rotor rim seal (bracketed by the two blue lines), were chosen for analysis.

Figures 3.4(a) and (b) show, respectively, the radial and tangential velocity radial distributions for the two 3° sectors. θ is defined as $(90-\phi)$, where ϕ is the azimuthal angle measured clockwise from the vertical centerline of the rotor. The average radial velocity is slightly less than zero before it moves upward (+) or downward (-) depending upon the circumferential sector. The negative radial velocities quite possibly correspond to the ingested main air. Conforming to the boundary condition at this axial position, the radial velocity becomes zero at the stator rim seal (as shown by the extrapolation dotted lines). It should be remarked that nine out of the ten vector files at this position showed two incoming radial velocity (red) regions compared to five out of ten at 2.6 mm from the stator. This may connote that much of the ingested flow remains very close to the stator surface. The tangential velocity, Fig. 3.4(b), increases inappreciably inboard of the rim cavity and with a steeper gradient as it approaches the rim seal. This higher tangential velocity near the rotor rim seal may be due to the combined effect of the rotor speed and the ingested main air which possesses high tangential velocity (as imparted by the vanes). It should be noted that the tangential velocity distribution overlaps for the two sectors under consideration.

Figures 3.5(a) and (b) show, respectively, for the same experimental condition the instantaneous velocity map and the corresponding radial velocity component map at 2.6 mm from the rotor surface. Because of the rotor in
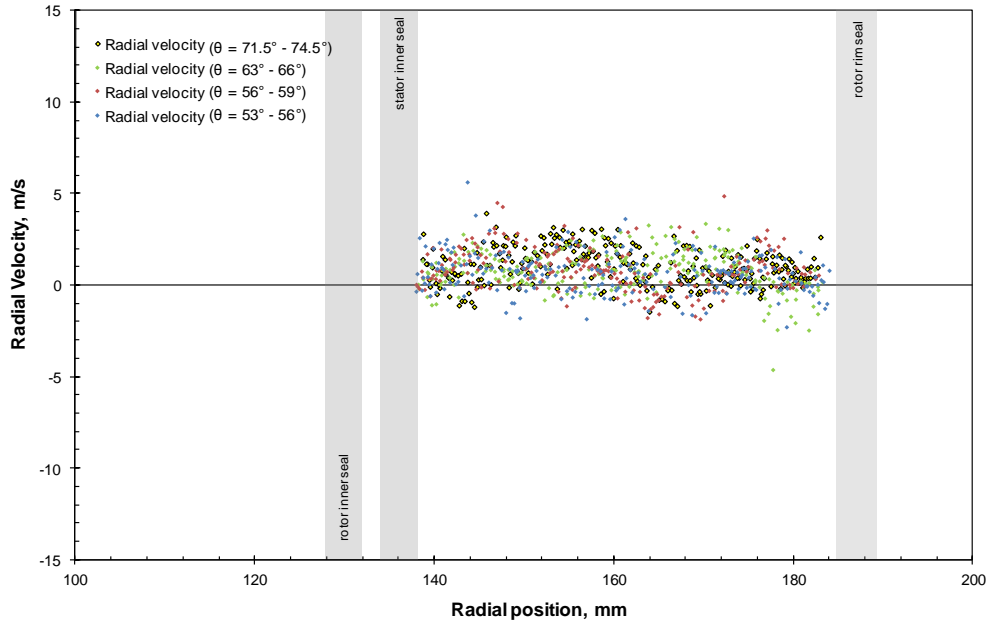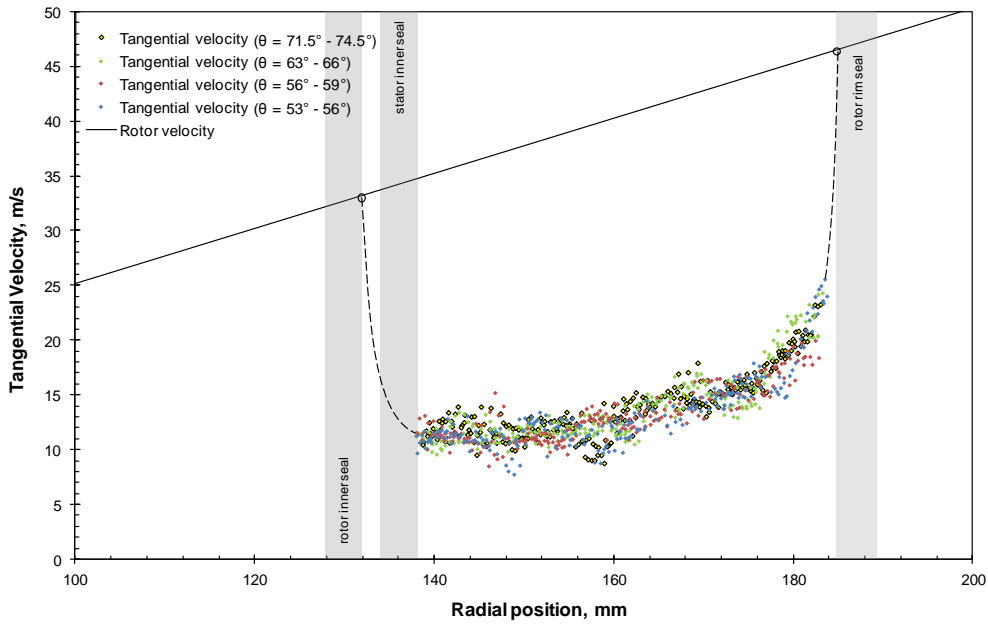
45

(a)   Instantaneous velocity

(b)   Instantaneous radial velocity

Fig. 3.5 r-ϕ plane instantaneous velocity vector maps in the rim cavity at 2.6 mm from the rotor surface – $Re_{vax} = 1.12 \times 10^5$, $Re_\phi = 6.14 \times 10^5$, $c_w = 1540$ ($\delta t = 15$ µs)

46
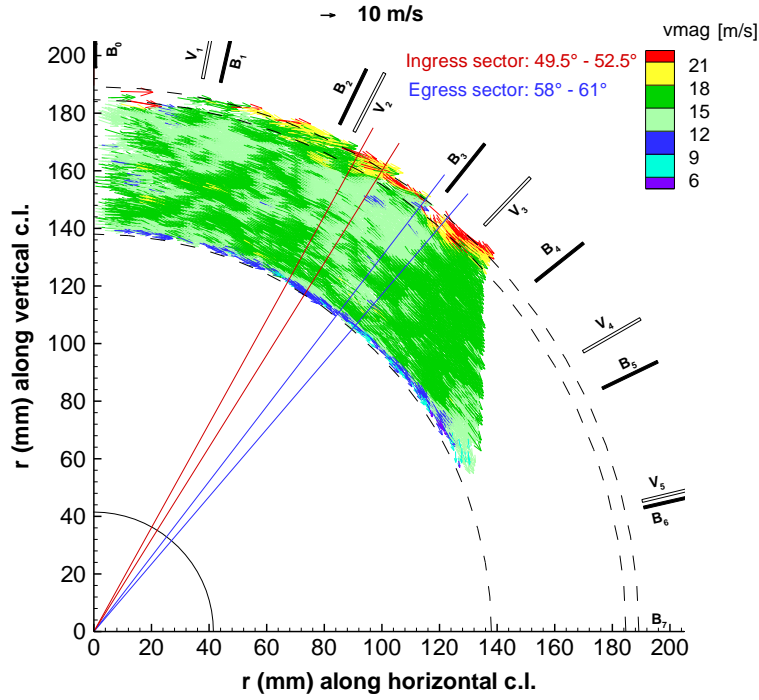
(a)   Radial Velocity

(b)   Tangential Velocity

Fig. 3.6   r-ϕ plane instantaneous radial and tangential velocities in the rim cavity at 2.6 mm from the rotor surface – $Re_{vax} = 1.12 \times 10^5$, $Re_\phi = 6.14 \times 10^5$, $c_w = 1540$ ($\delta t = 15$ µs)

47

background, it was difficult to obtain a velocity map without some erroneous vectors provided by oil droplets sticking to the rotor surface. After their deletion, a few small areas devoid of vectors can be seen in Fig. 3.5(a). The average velocity at each radius appears to have decreased in comparison to the vector map at 1.9 mm from the stator. At 2.6 mm from the rotor, four 3° sectors were selected to obtain the instantaneous radial and tangential velocity distributions, Figs. 3.6(a) and (b).

Figure 3.6(a) indicates that for all the four sectors, the radial velocity remains positive over the radius range, though low in magnitude. This is possibly due to the combined effects of rotor disk pumping and the purge air exiting the labyrinth seal gap. The tangential velocity, Fig. 3.6(b), is the dominant velocity component at this low purge air flow rate. Near the rotor rim seal the tangential velocity increases with a steep gradient. Here, the boundary conditions for the tangential velocity at the labyrinth seal and the rotor rim seal are the rotor velocities at their respective radii.

Case of $Re_{vax} = 1.12 \times 10^5$, $Re_\phi = 6.14 \times 10^5$, $c_w = 3080$

Figures 3.7(a) and (b) depict the r-ϕ instantaneous velocity and its radial component vector maps for this experimental condition at 1.9 mm from the stator surface. At this intermediate purge flow rate, a weak radial inflow is seen along with some suppression of the tangential velocity compared to the $c_w = 1540$ case. The high tangential velocity (red) region seen for $c_w = 1540$ at this same axial location are sparsely observed. The velocity bands are also no longer seen. The radial and tangential velocities for two selected sectors are shown in Fig. 3.8(a)

(a)   Instantaneous velocity
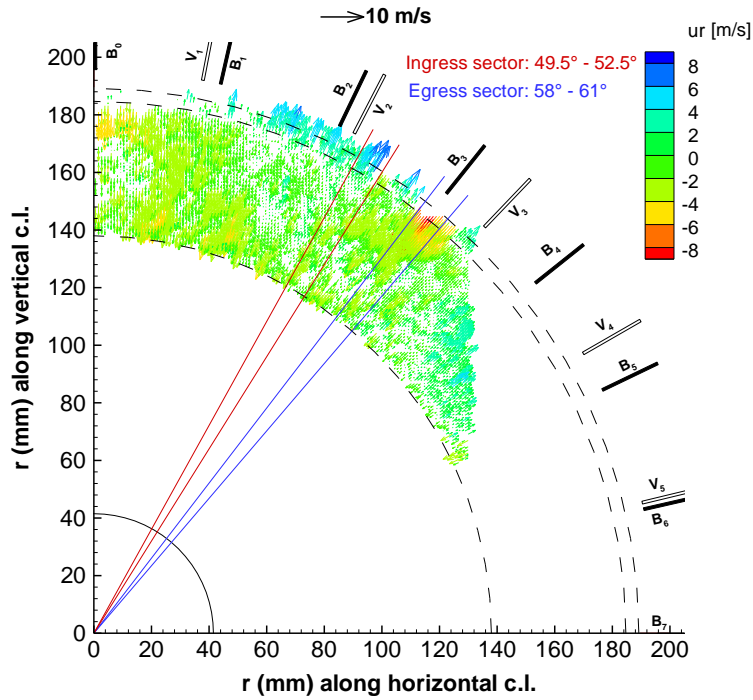
(b)   Instantaneous radial velocity

Fig. 3.7 r-φ plane instantaneous velocity vector maps in the rim cavity at 1.9 mm from the stator surface – $Re_{vax} = 1.12 \times 10^5$, $Re_\phi = 6.14 \times 10^5$, $c_w = 3080$ ($\delta t = 12$ μs)
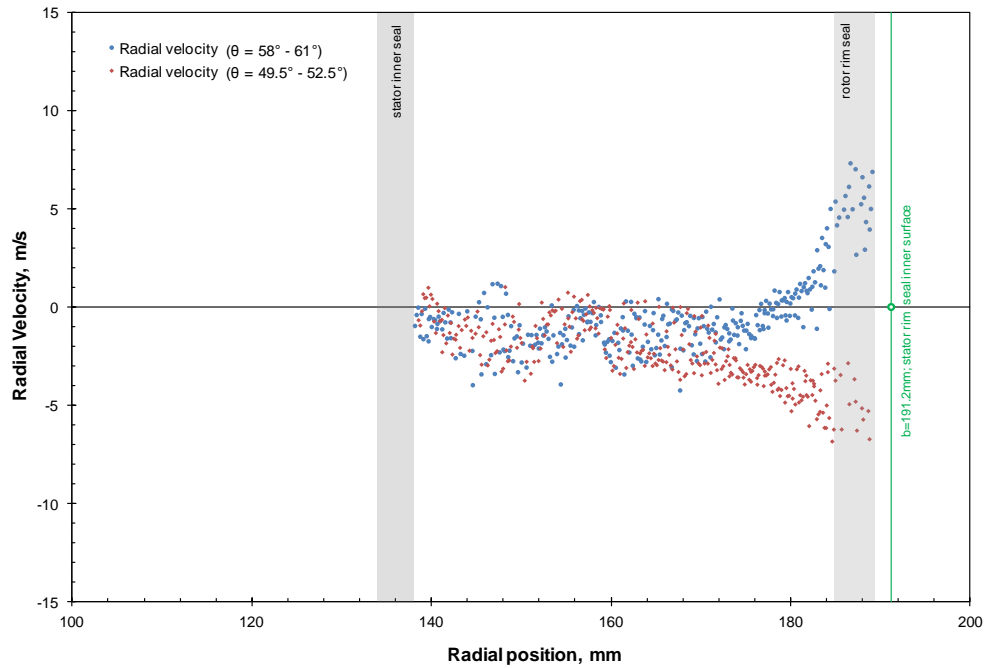
49

and (b). The radial velocity for both sectors is negative till r = 172 mm, after which it becomes more negative or positive depending on the sector. The tangential velocity slightly dips as we proceed along the radius but increases markedly very close to the rotor rim seal.

At 2.6 mm from the rotor surface, Figs. 3.9(a) and (b), radial outflow can be clearly seen. Also, a decrease in the velocity magnitude in the entire flow field is observed as compared to at 1.9 mm from the stator surface. For the four sectors selected for analysis, the radial velocity, Fig. 3.10(a), rises gradually along the radius in the inboard half of the rim cavity and then decreases in the outer half – reducing toward zero as the rotor rim seal is approached. The tangential velocity distribution, Fig. 3.10(b), is quite flat at this higher purge air flow rate.

Case of $Re_{vax} = 1.12 \times 10^5$, $Re_\phi = 6.14 \times 10^5$, $c_w = 4261$

Figures 3.11(a) and (b) show the velocity vector maps for, respectively, the instantaneous velocity and its radial component at 1.9 mm from the stator surface for this experimental condition. These plots have regions devoid of vectors especially near the rim seal due to the rapid out-of-plane (axial) movement of the cavity air at the high purge air flow rate. In Fig. 3.11(b), distinct pockets of negative radial velocities separated by egress sectors can be seen with large magnitude negative radial velocities (red vectors) at the center of these pockets. As shown in Fig. 3.12(a), the radial velocity for both the selected sectors is mostly negative in the rim cavity, its magnitude increasing along the radius till the middle of the cavity after which the magnitude decreases, tending toward zero as the rotor rim seal is approached. In the rim seal region, the radial velocity
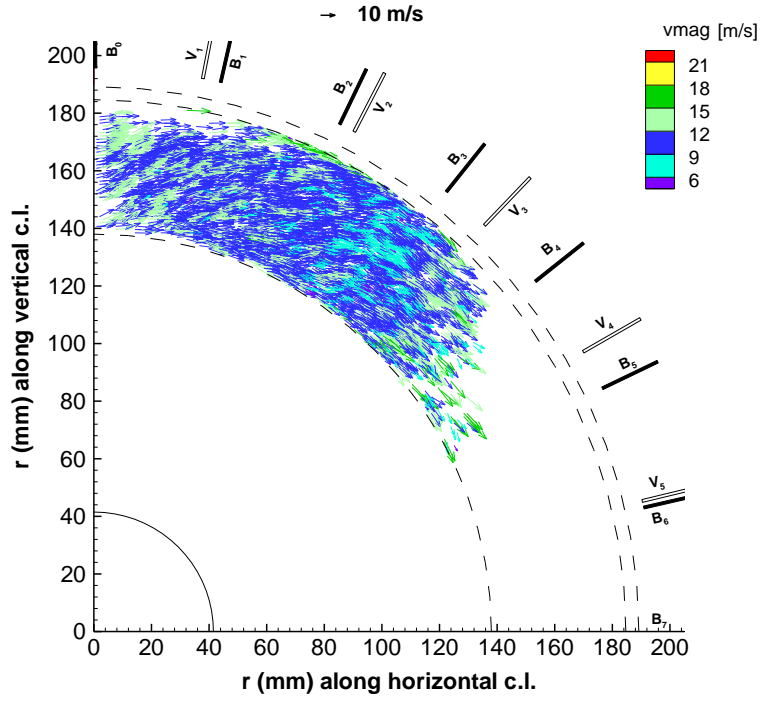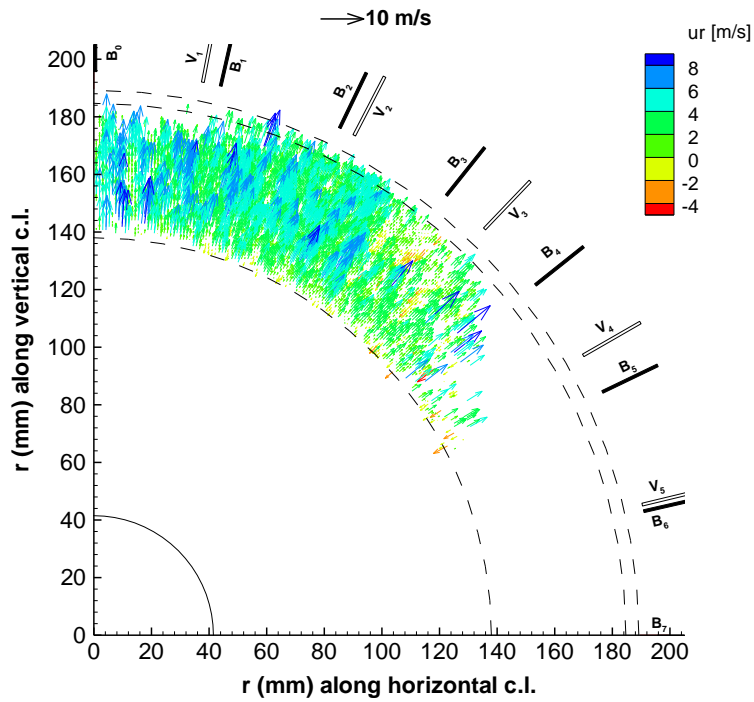
50

(a)   Radial Velocity

(b)   Tangential Velocity

Fig. 3.8 r-ϕ plane instantaneous radial and tangential velocities in the rim cavity at 1.9 mm from the stator surface − $Re_{vax} = 1.12 \times 10^5$, $Re_\phi = 6.14 \times 10^5$, $c_w = 3080$ ($\delta t = 12$ μs)
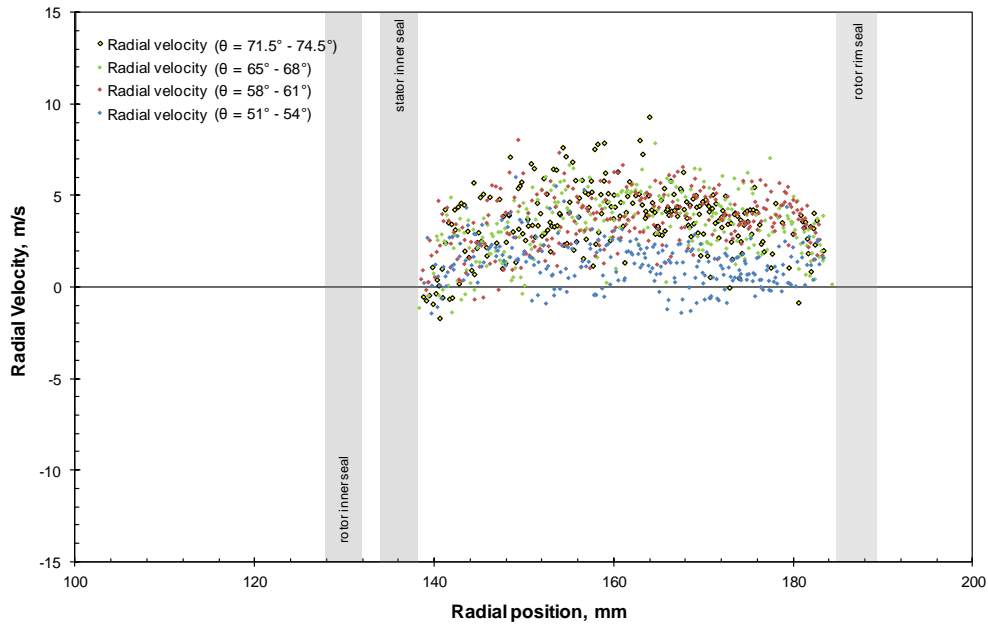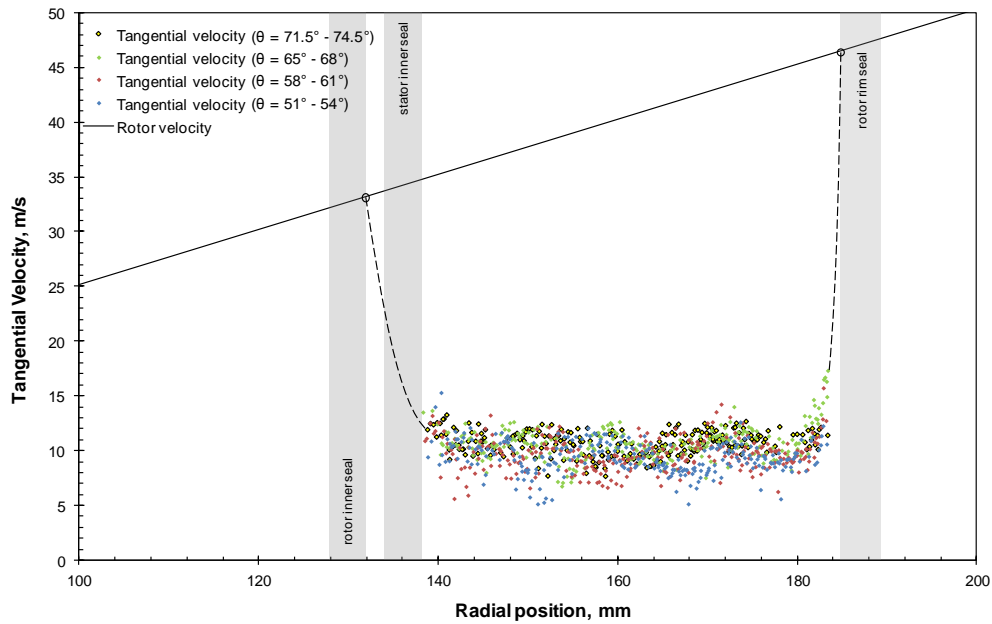
51

(a)   Instantaneous velocity

(b)   Instantaneous radial velocity

Fig. 3.9 r-ϕ plane instantaneous velocity vector maps in the rim cavity at 2.6 mm from the rotor surface – $Re_{vax} = 1.12{\times}10^5$, $Re_{\phi} = 6.14{\times}10^5$, $c_w = 3080$ ($\delta t = 12$ μs)
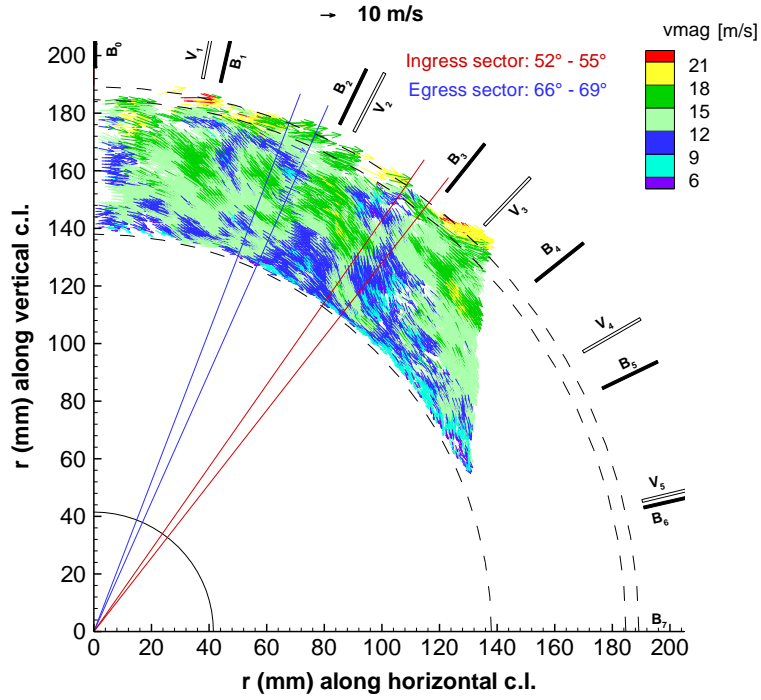
(a)   Radial Velocity
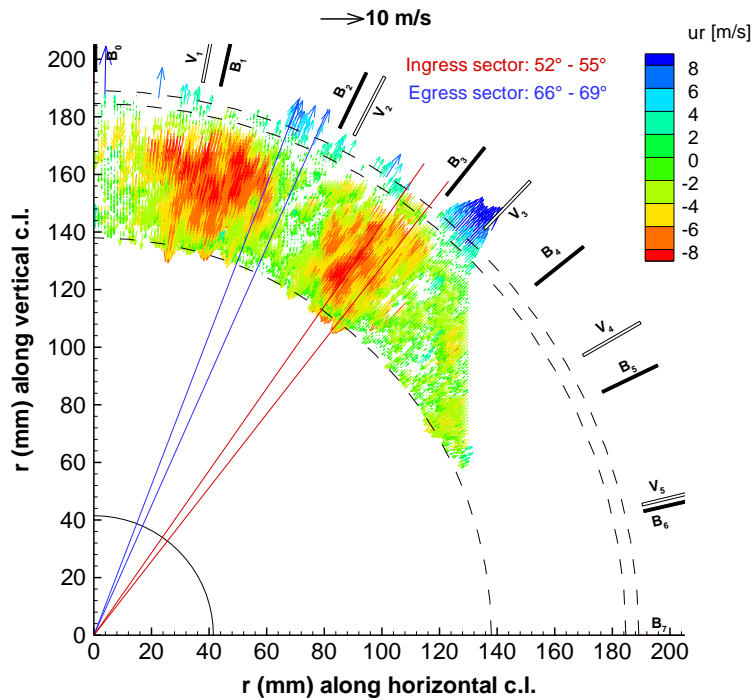

(b)   Tangential Velocity

Fig. 3.10 r-ϕ plane instantaneous radial and tangential velocities in the rim cavity at 2.6 mm from the rotor surface – $Re_{vax} = 1.12 \times 10^5$, $Re_\phi = 6.14 \times 10^5$, $c_w = 3080$ ($\delta t = 12$ µs)

53

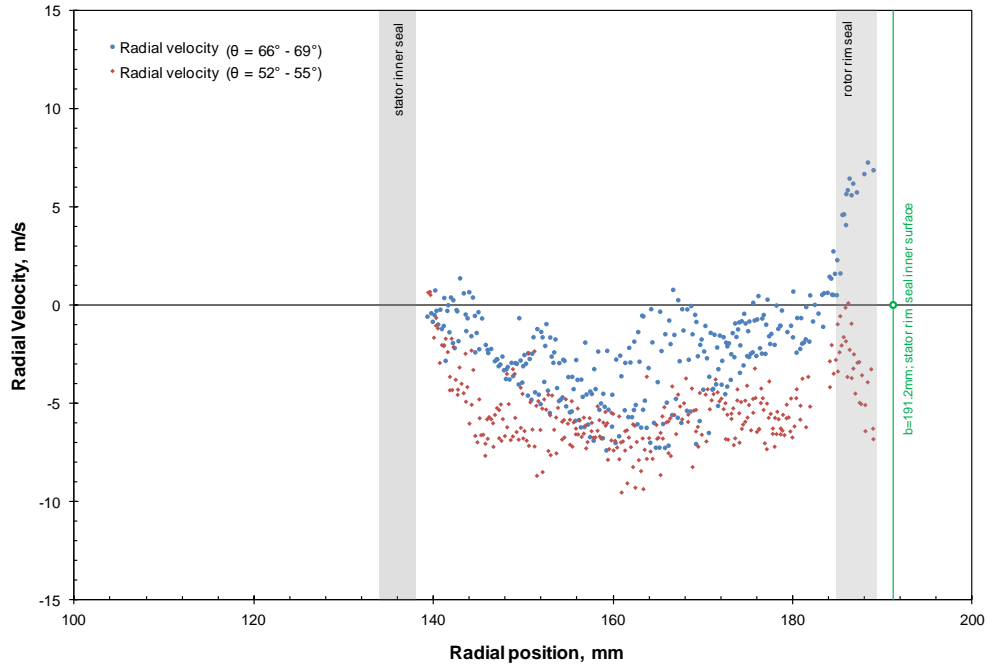(a)   Instantaneous velocity

(b)   Instantaneous radial velocity

Fig. 3.11 r-ϕ plane instantaneous velocity vector maps in the rim cavity at 1.9 mm from the stator surface – $Re_{vax} = 1.12 \times 10^5$, $Re_{\phi} = 6.14 \times 10^5$, $c_w = 4621$ ($\delta t = 12$ μs)

separates out depending on the sector (egress or ingress). The flat tangential velocity distributions for the two sectors, Fig. 3.12(b), do not overlap in the mid-rim cavity region – the ingress sector shows a decrease in the tangential velocity. Closer to the rotor rim seal, the tangential velocity shows a slight increase for both sectors.

Figures 3.13(a) and (b) shows the instantaneous velocity vector maps for the same experimental condition at 2.6 mm from the rotor surface. Figure 3.14(a) depicts the dome-shaped distribution of the radial velocity. In the mid-rim cavity region, high radial velocity – comparable to the tangential velocity, Fig. 3.14(b), is observed. The tangential velocity indicates considerable scatter. The average tangential velocity is essentially flat across the entire rim cavity.

Ensemble-Circumferential-Averages

Figures 3.15(a), 3.16(a) and 3.17(a) show the ensemble-circumferential-average radial velocity distribution at all axial locations for the experiment set II and c_w = 1540, 3080 and 4621. The instantaneous radial velocities, for the near stator locations, Figs. 3.4(a), 3.8(a) and 3.12(a), move upward or downward near the rim seals depending upon the circumferential sector. The ensemble-circumferential-averaging smoothens out this variation. However, inboard of the rim cavity, the instantaneous radial velocities do not vary circumferentially. Hence, ensemble-circumferential-averaging provides a much accurate trend of the fluid radial velocities inboard of the rim cavity, which are helpful in developing the qualitative streamline flow patterns presented later.
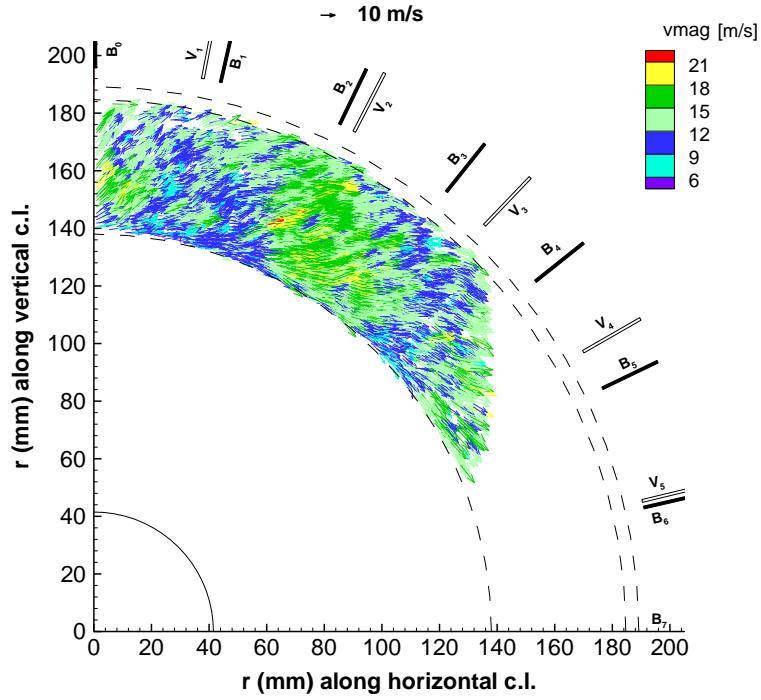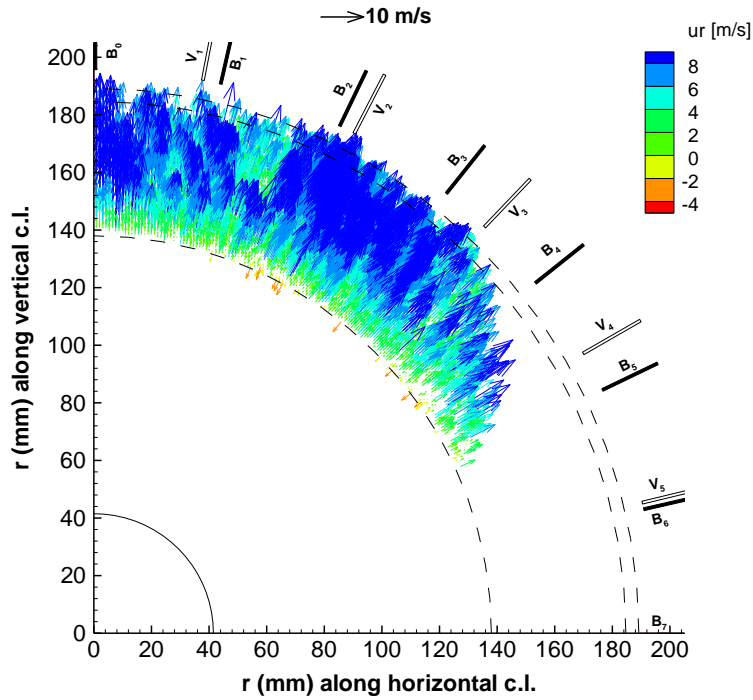
(a)   Radial Velocity
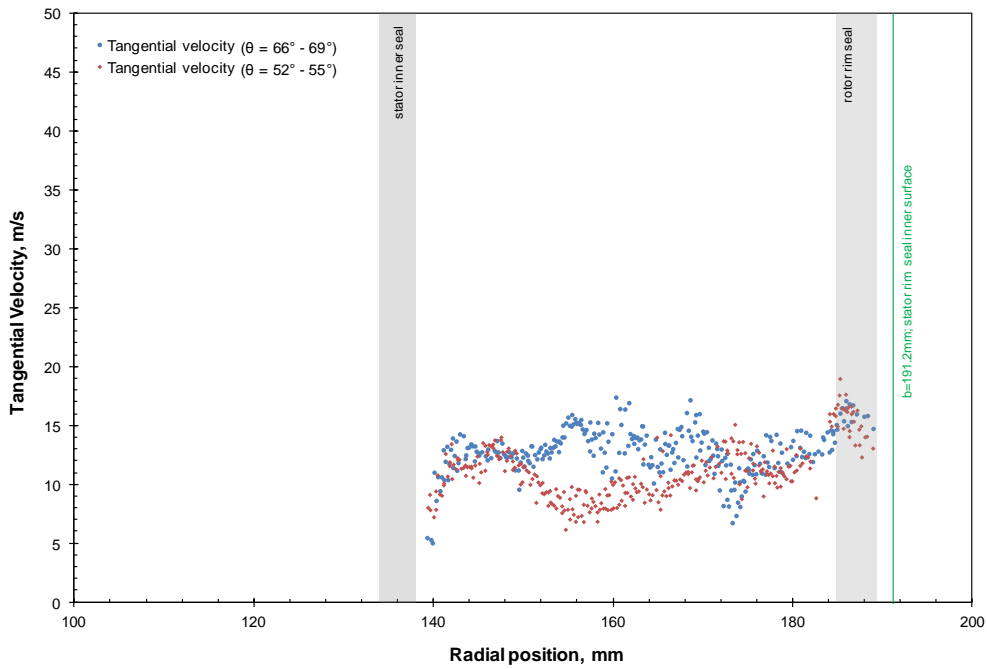
(b)   Tangential Velocity

Fig. 3.12 r-ϕ plane instantaneous radial and tangential velocities in the rim cavity at 1.9 mm from the stator surface – $Re_{vax} = 1.12 \times 10^5$, $Re_\phi = 6.14 \times 10^5$, $c_w = 4621$ ($\delta t = 12$ μs)
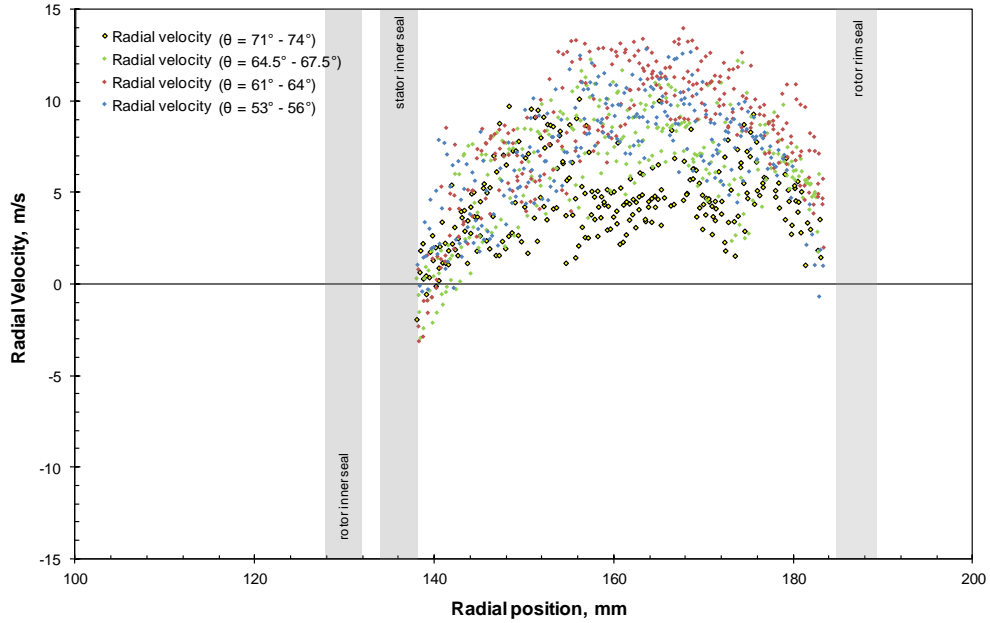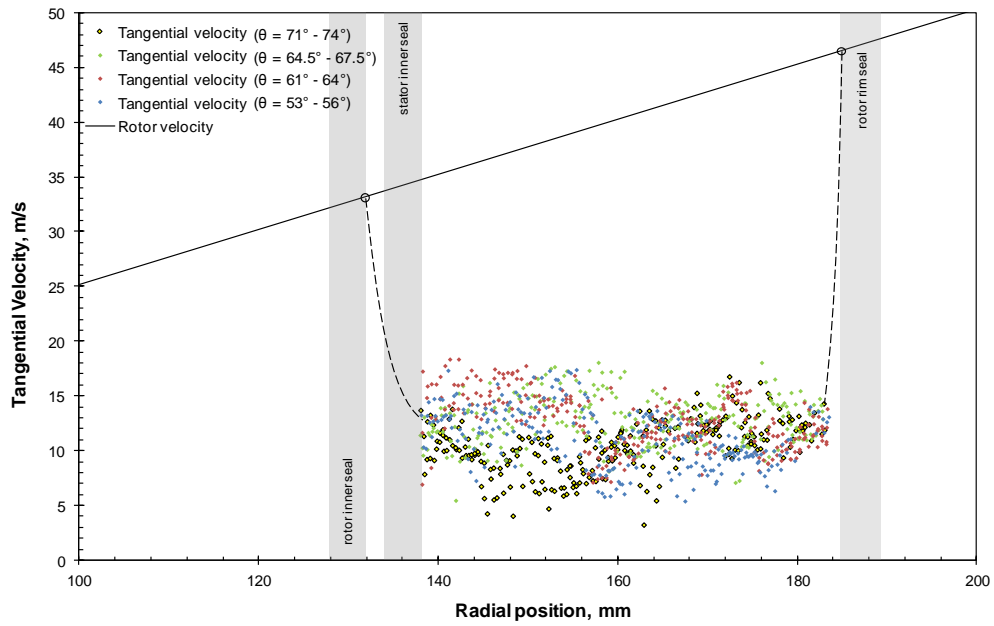
(a)   Instantaneous velocity

(b)   Instantaneous radial velocity

Fig. 3.13 r-ϕ plane instantaneous velocity vector maps in the rim cavity at 2.6 mm from the rotor surface $-$ $Re_{vax} = 1.12 \times 10^5$, $Re_\phi = 6.14 \times 10^5$, $c_w = 4621$ ($\delta t = 12$ µs)
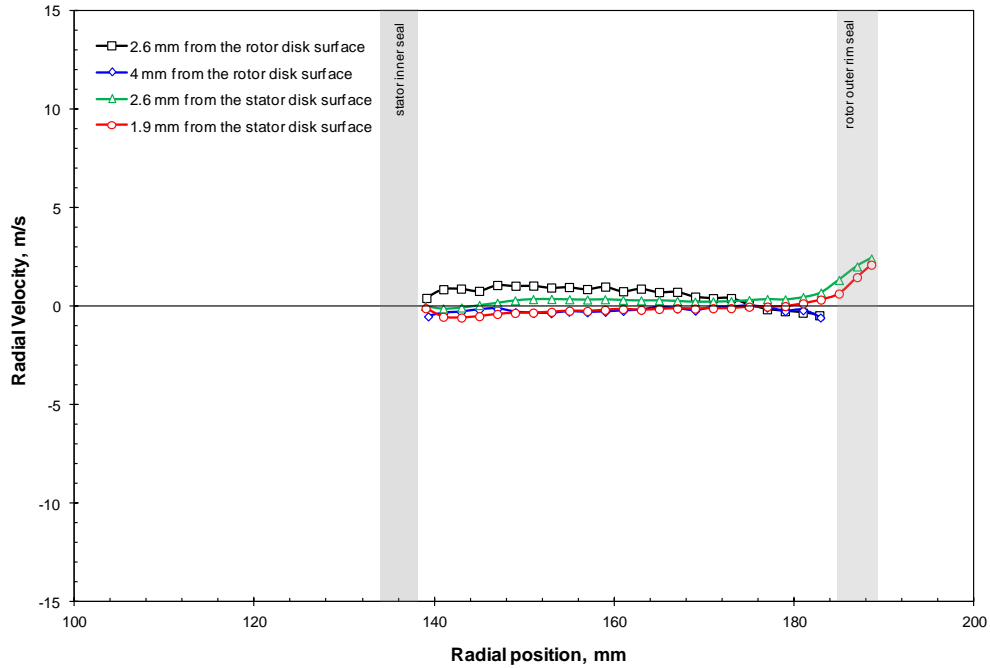
(a)   Radial Velocity

(b)   Tangential Velocity

Fig. 3.14 r-ϕ plane instantaneous radial and tangential velocities in the rim cavity at 2.6 mm from the rotor surface − $Re_{vax} = 1.12 \times 10^5$, $Re_\phi = 6.14 \times 10^5$, $c_w = 4621$ ($\delta t = 12$ μs)

(a)   Radial Velocity

(b)   Tangential Velocity

Fig. 3.15 Effect of axial measurement position on circumferential-average velocity in the rim cavity obtained from ensemble-averaged r-ϕ plane velocity vector maps – $Re_{vax} = 1.12 \times 10^5$, $Re_{\phi} = 6.14 \times 10^5$, $c_w = 1540$

(a)   Radial Velocity

(b)   Tangential Velocity

Fig. 3.16 Effect of axial measurement position on circumferential-average velocity in the rim cavity obtained from ensemble-averaged r-ϕ plane velocity vector maps – $Re_{vax} = 1.12 \times 10^5$, $Re_\phi = 6.14 \times 10^5$, $c_w = 3080$
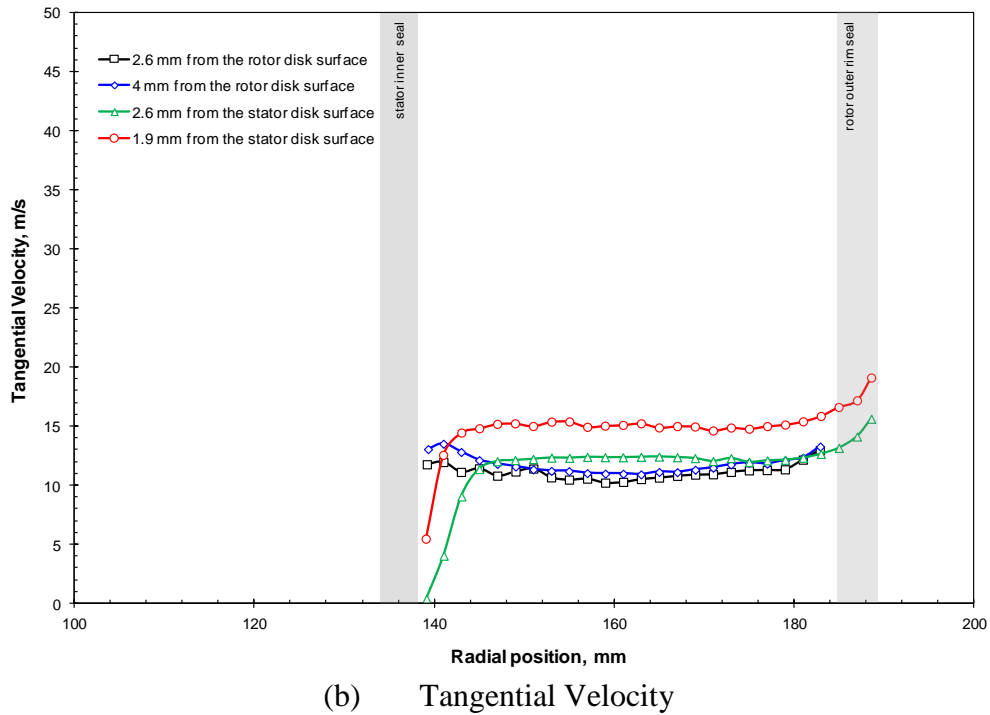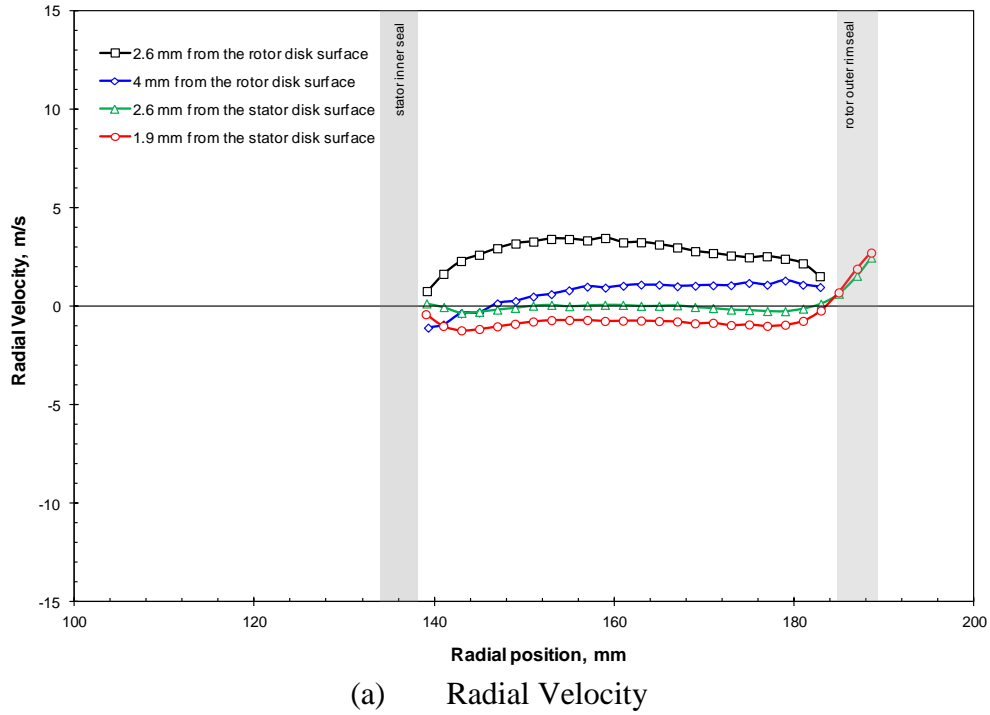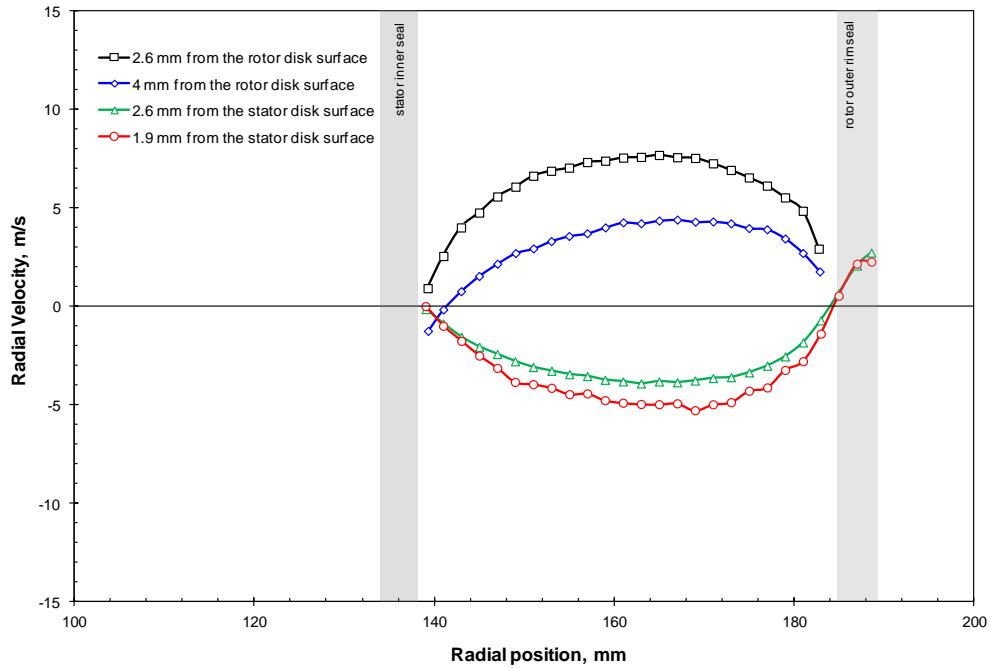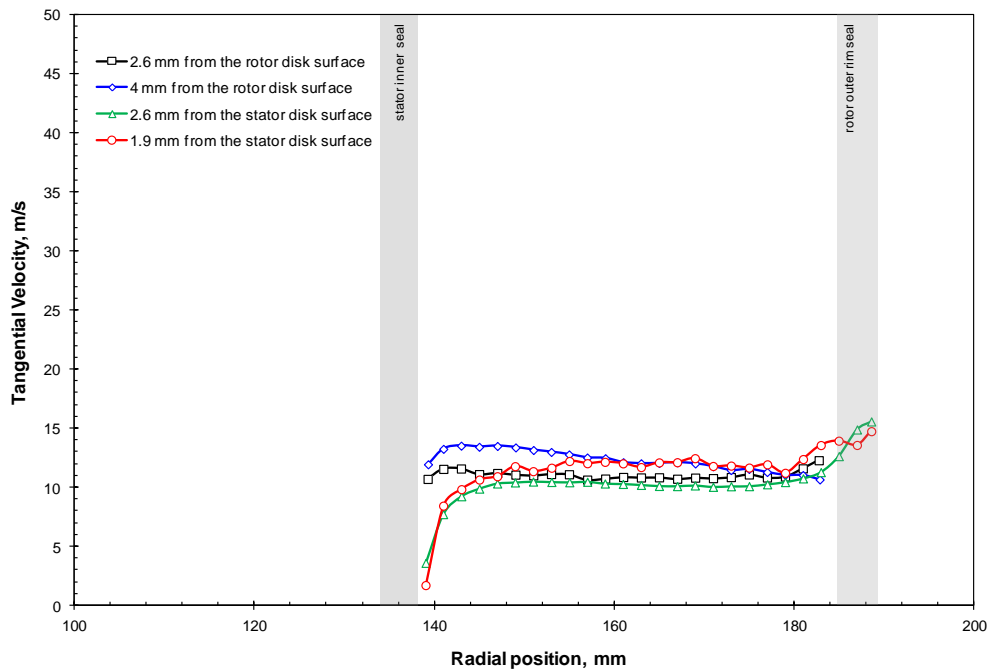
60

(a)   Radial Velocity

(b)   Tangential Velocity

Fig. 3.17 Effect of axial measurement position on circumferential-average velocity in the rim cavity obtained from ensemble-averaged r-ϕ plane velocity vector maps – $Re_{vax} = 1.12 \times 10^5$, $Re_\phi = 6.14 \times 10^5$, $c_w = 4621$

61

In the rim cavity, Figs. 3.15(a), 3.16(a) and 3.17(a), the radial velocity near the rotor surface becomes more positive and the radial velocity near the stator surface becomes more negative as the purge flow rate increases. This is attributed to the formation of a recirculation region. The negative radial velocity observed at 4 mm from the rotor surface near the vicinity of the stator inner seal for all purge flow rates should be noted. This quite possibly indicates that the flow is entering the inner cavity from the stator inner seal lip.

The ensemble average tangential velocities are shown in Figs. 3.15 (b), 3.16 (b) and 3.17 (b). The unexpected higher tangential velocities seen at the near stator surface locations compared to those at the near rotor surface locations for $c_w = 1540$ and 3080 might be due to the ingested main air which possesses higher tangential velocity than the indigenous cavity air. An overall suppression of tangential velocity in the outboard region of the rim cavity with increase in purge flow rate can be seen.

Figures 3.18 to 3.20 show the ensemble average radial and tangential velocities for experiment set I. The magnitudes of the radial velocity in the rim cavity are slightly higher than those seen for experiment set II for the corresponding purge flow rate. This is due to the higher purge flow rate to main flow rate ratio and the reduction in the rotor speed. The tangential velocities show similar trend as shown for experiment set II except their magnitudes are considerably lower due to the lower rotor speed.

(a)   Radial Velocity

(b)   Tangential Velocity

Fig. 3.18 Effect of axial measurement position on circumferential-average velocity in the rim cavity obtained from ensemble-averaged r-ϕ plane velocity vector maps – $Re_{vax} = 9.27 \times 10^4$, $Re_\phi = 4.85 \times 10^5$, $c_w = 1540$

(a)   Radial Velocity

(b)   Tangential Velocity

Fig. 3.19 Effect of axial measurement position on circumferential-average velocity in the rim cavity obtained from ensemble-averaged r-ϕ plane velocity vector maps – $\mathrm{Re_{vax}} = 9.27 \times 10^4$, $\mathrm{Re_\phi} = 4.85 \times 10^5$, $c_w = 3080$
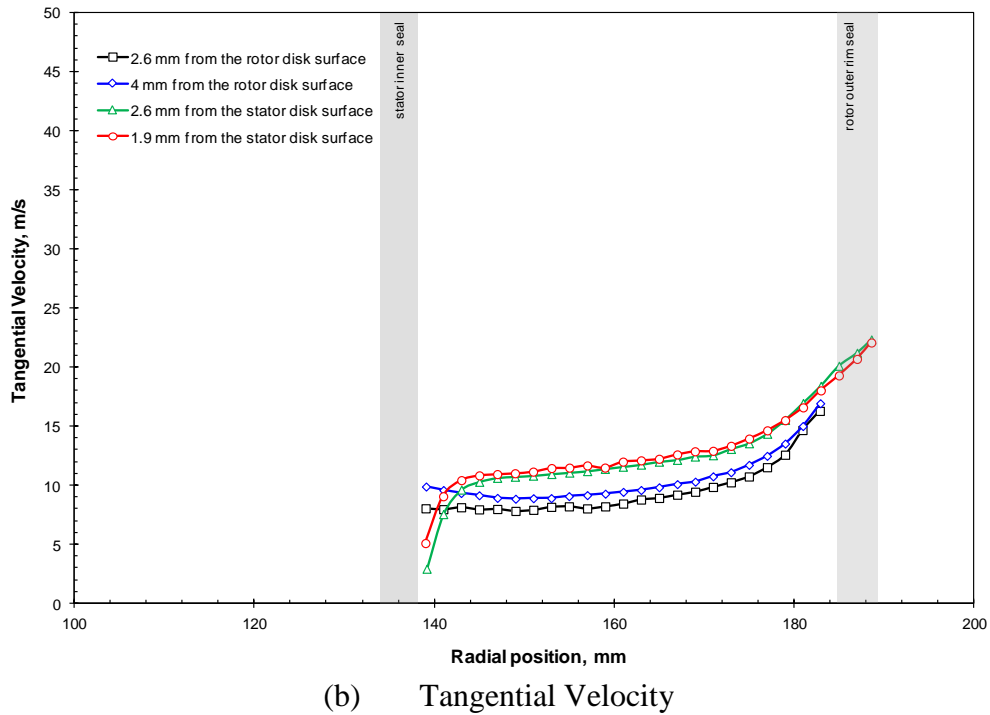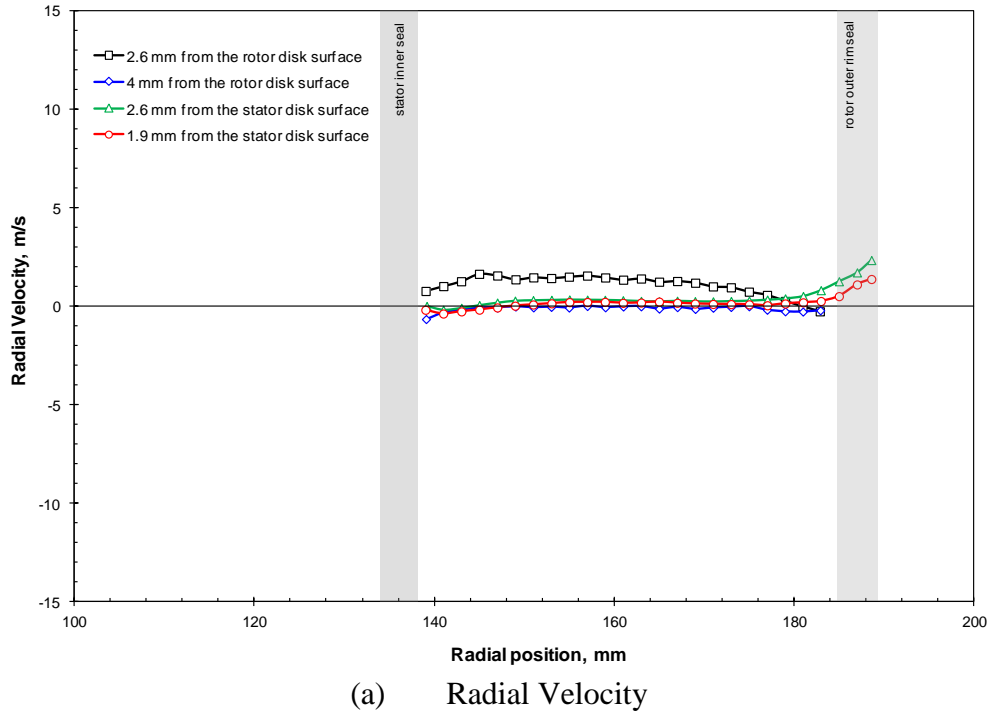
(a)   Radial Velocity

(b)   Tangential Velocity
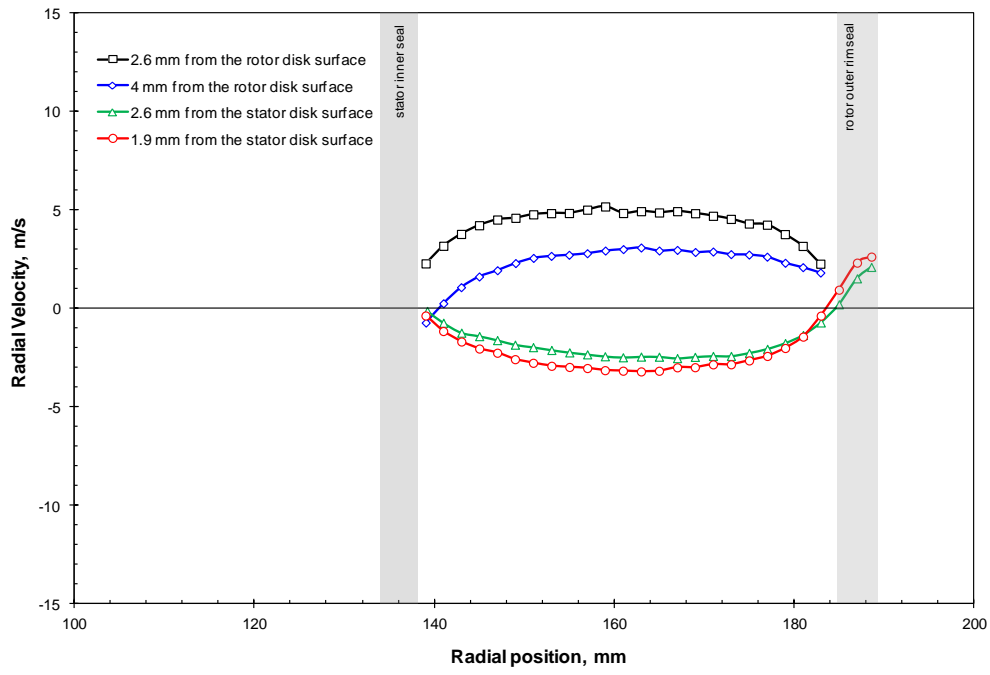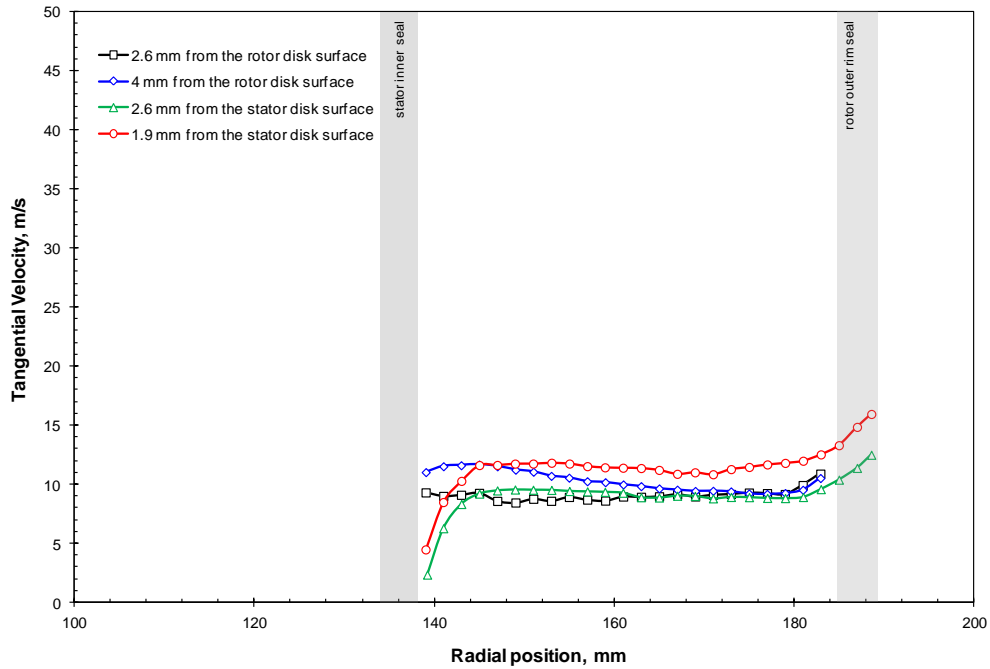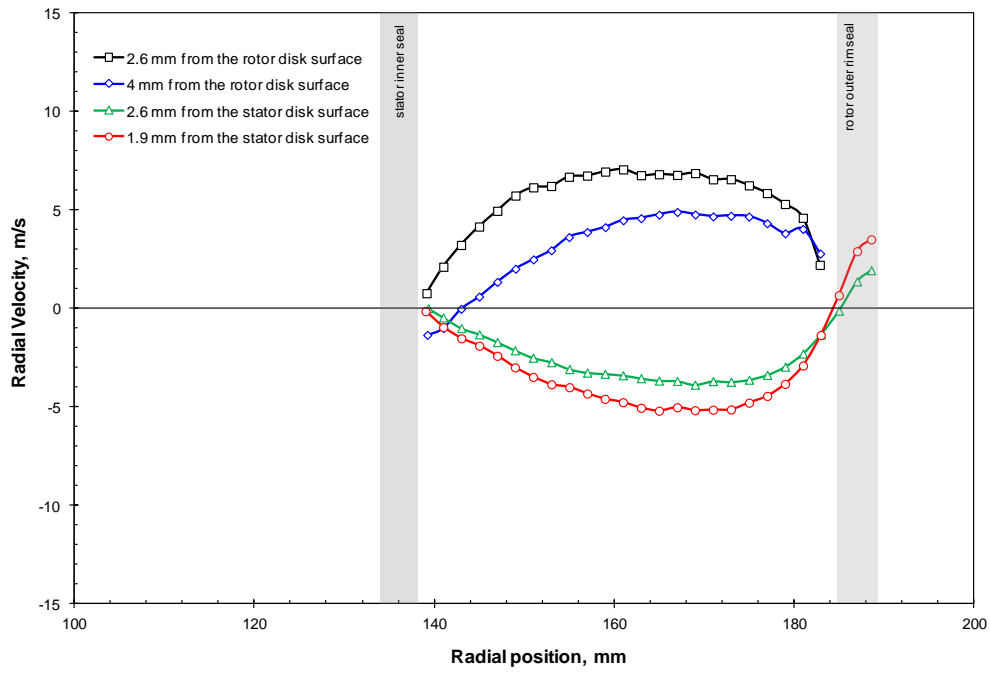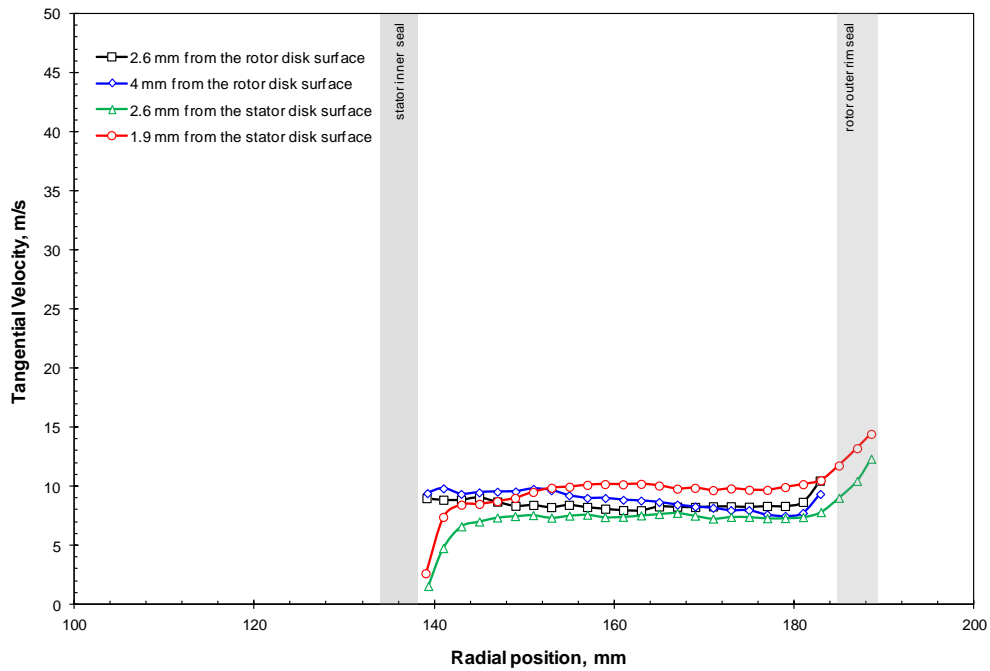
Fig. 3.20 Effect of axial measurement position on circumferential-average velocity in the rim cavity obtained from ensemble-averaged r-ϕ plane velocity vector maps – $Re_{vax} = 9.27 \times 10^4$, $Re_{\phi} = 4.85 \times 10^5$, $c_w = 4621$

65

3.4   Relating the Measured Velocity Field to the Static Pressure and Ingestion Distributions

For this particular configuration, along with the static-gage pressure and PIV measurements, ingestion of mainstream gas was also measured at the stator surface as well as at some locations in the cavity. Though these ingestion measurements do not form a part of this thesis, they play an important part in quantifying the main gas ingestion and understanding the flow field inside the rim cavity. Figure 3.21 shows the distribution of sealing effectiveness on the stator surface for the experiment set II. A brief summary of the ingestion distribution results is given below:

1.   The sealing effectiveness in the rim cavity increases as the purge air flow rate increases.

2.   In the inner cavity the overall sealing effectiveness is relatively high but it decreases slightly with increase in purge air flow rate.

3.   The sealing effectiveness values for experiment set I are a marginally higher than observed for experiment set II.

For $c_w = 1540$, the sealing effectiveness values remain constant at around 0.80 till $r \approx 162$ mm after which a gradual decrease is found as the rim seal is approached. The constant values of sealing effectiveness would suggest the existence of a well mixed region. Even the analysis of the instantaneous vector file, obtained at 4 mm from the stator, shows a separation of the ingress and egress sector radial velocities at around the radius of 162 mm. These findings and Fig. 3.15(a) point out towards a weak recirculation region radially inboard in the

66

rim cavity. Figures 3.22(a) and (b) show, qualitatively, separate flow streamline sketches in the r-x plane for an egress sector and an ingress sector.
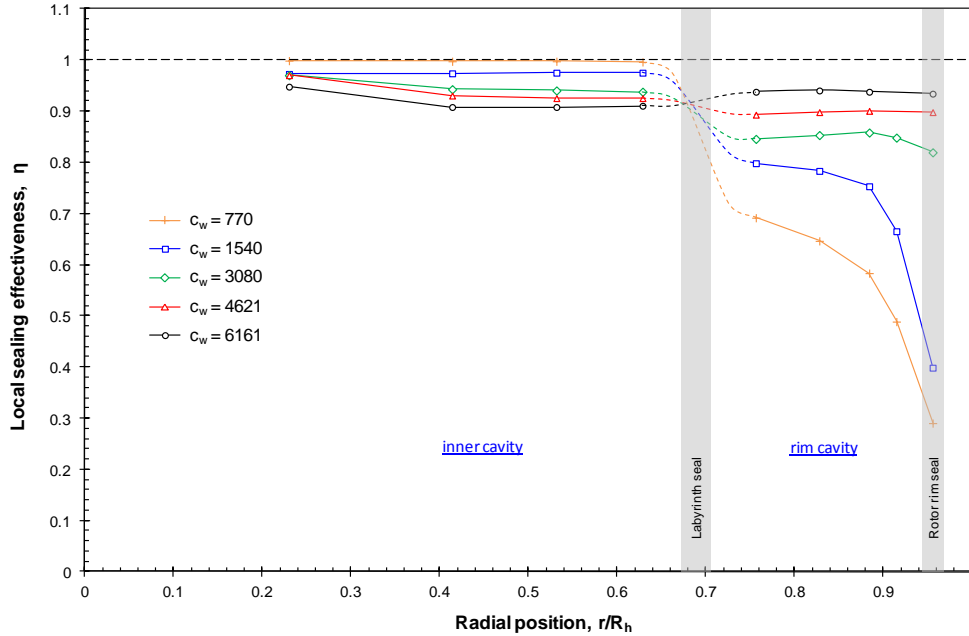
Fig. 3.21 Radial distribution of sealing effectiveness at the stator disk surface – $Re_{vax} = 1.12 \times 10^5$, $Re_\phi = 6.14 \times 10^5$

On similar lines, for $c_w = 3080$ the sealing effectiveness in the rim cavity remains constant at 0.90 till r ≈ 172 mm after which it decreases steadily with the radius. In the instantaneous PIV map, Fig. 3.8(a), the ingress and egress radial velocities branch out at about the same radius. Thus, a recirculation region extending further up the radius can be anticipated as depicted in Figs. 3.23(a) and (b).

For c_w = 4621, Figs. 3.21 and 3.17(a), the presence of a strong recirculation region extending over the entire rim cavity can be inferred; this is shown in Figs. 3.24(a) and (b).
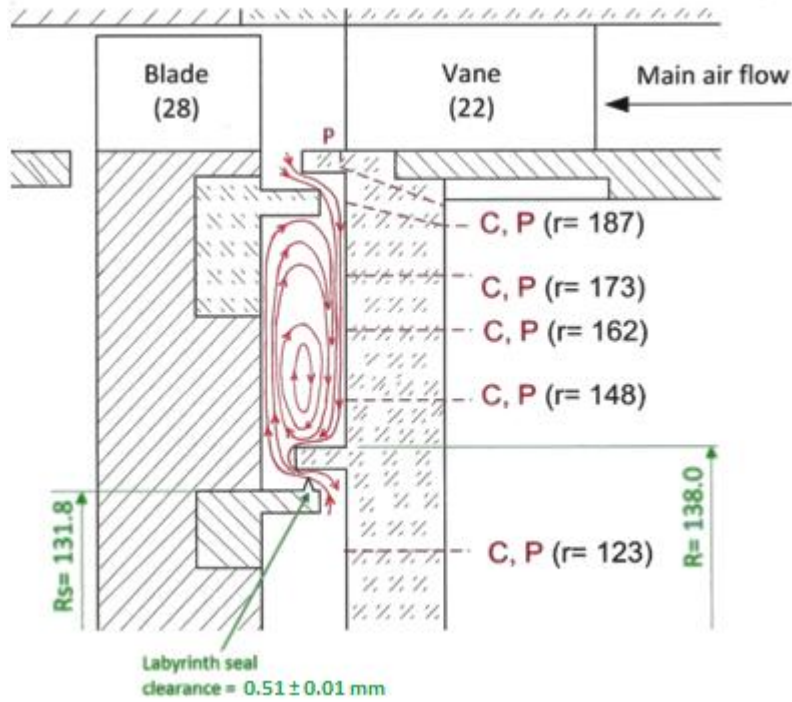
(a)   Ingress Sector
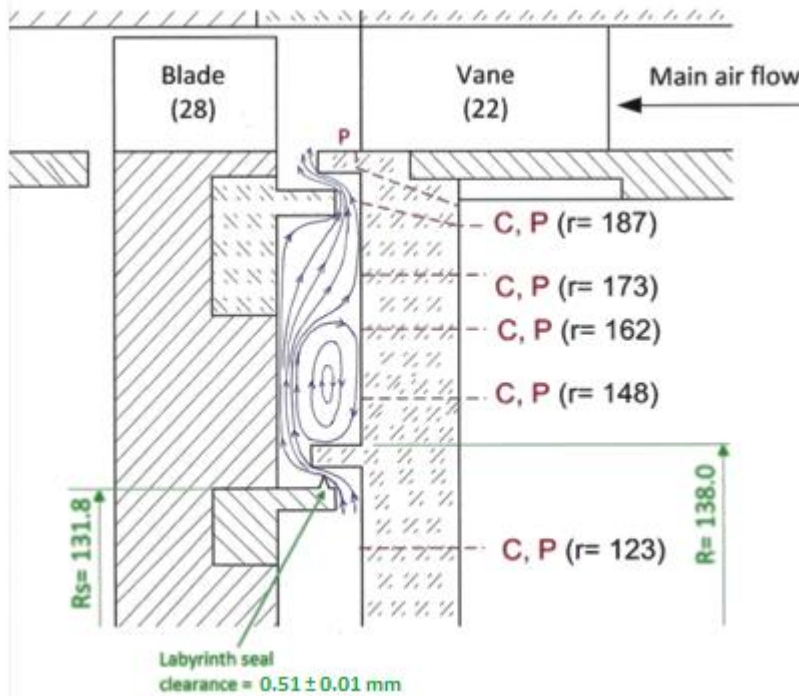
(b)   Egress Sector

Fig. 3.22 Qualitative streamline flow patterns in the r-x plane – $Re_{vax} = 1.12 \times 10^5$, $Re_\phi = 6.14 \times 10^5$, $c_w = 1540$

(a)   Ingress Sector
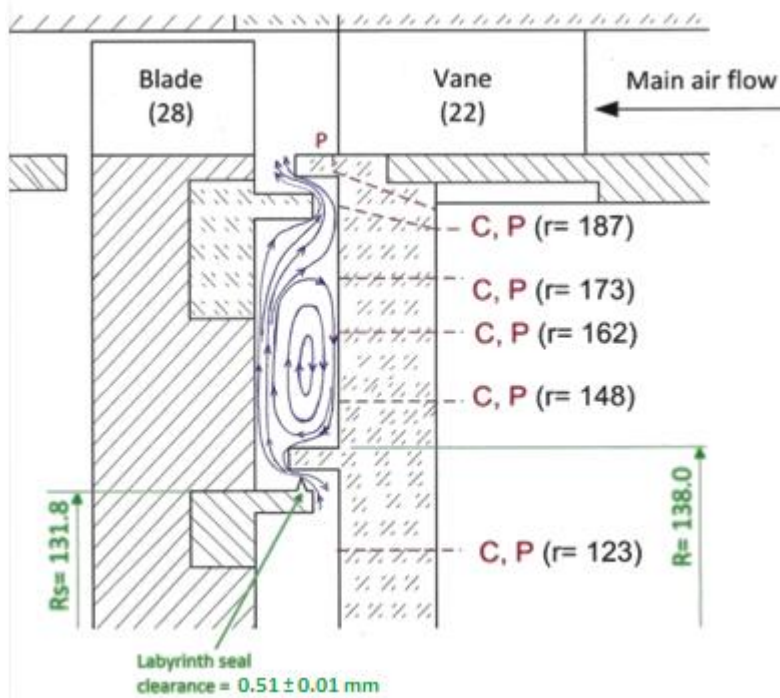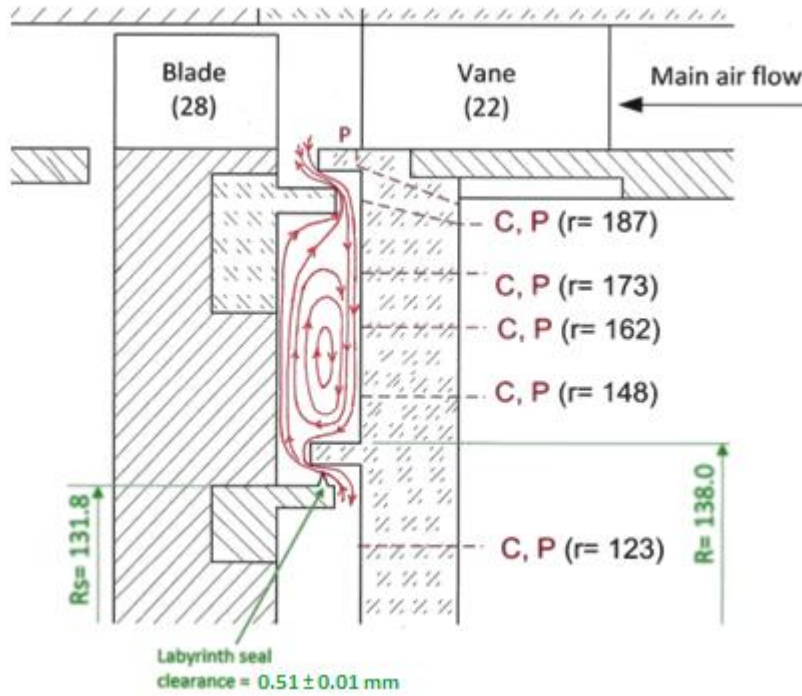
(b)   Egress Sector

Fig. 3.23 Qualitative streamline flow patterns in the r-x plane – $Re_{vax} = 1.12 \times 10^5$, $Re_\phi = 6.14 \times 10^5$, $c_w = 3080$
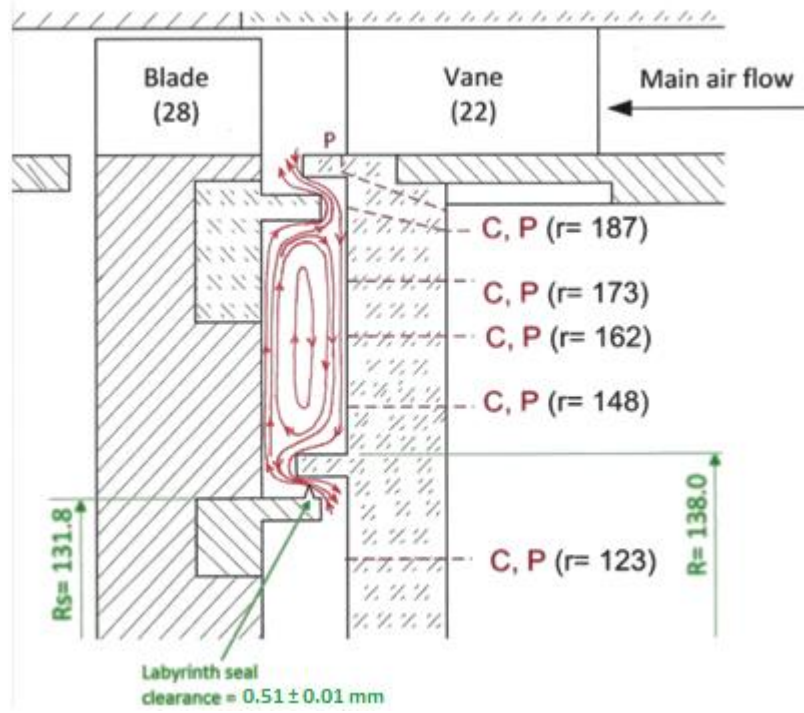
(a)   Ingress Sector
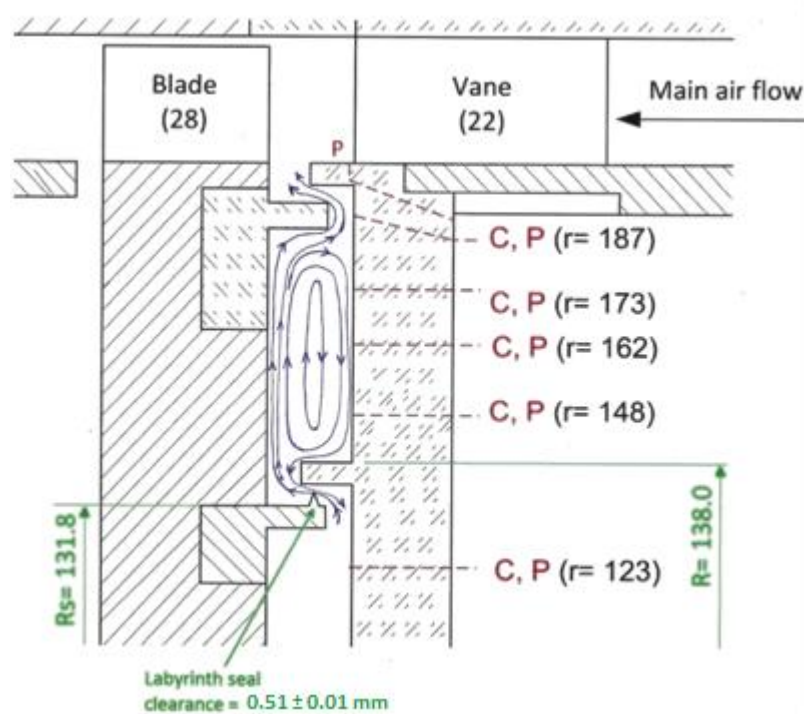
(b)   Egress Sector

Fig. 3.24 Qualitative streamline flow patterns in the r-x plane – $Re_{vax} = 1.12 \times 10^5$, $Re_\phi = 6.14 \times 10^5$, $c_w = 4621$

In the PIV maps, negative radial velocities are seen at 4 mm from the rotor in the vicinity of the stator inner seal for all of the experimental conditions. The 'sharpness' of the radial velocity going from positive value to negative value as the inner seal is approached at this axial plane should be noted. This quite possibly indicates that there is flow entering the inner cavity from near the stator inner seal lip – a possible justification for the observed drop in sealing effectiveness in the inner cavity with increasing c_w, Fig. 3.21. This may have been caused by the presence of unsteady low-pressure structures in the outer region of the inner cavity.

Chapter 4

CONCLUSION

4.1   Concluding Remarks

Results have been reported for experiments in which time-average static pressure distribution in the main gas path and disk cavity and instantaneous fluid velocity field in the disk rim cavity were measured in a model single-stage axial flow turbine. Two different sets of rotor speed and mainstream gas flow rate, and several purge air flow rates were investigated. The main gas path featured vanes and blades; the disk cavity featured rim seals on the rotor disk and the stator with radial clearance and axial overlap as well as an inner labyrinth seal.

The static pressure in the main gas path annulus showed circumferentially periodic variation following the vane pitch. This pressure asymmetry produced by the vanes increased approximately quadratically with the mainstream air flow rate and was found to be maximum on the outer shroud immediately downstream of the vane trailing edge, its strength decaying gradually toward the blades. In the disk cavity, no periodic variation in pressure was found, indicating that the main gas path pressure asymmetry dissipated across the rim seals. The static pressure in the inner cavity (i.e., inboard of the labyrinth seal) increased substantially with increasing purge air flow rate, dropping down to a small range of lower pressures outboard of the labyrinth seal for all purge air flow rates. It was also observed that a higher purge air flow rate lowered the pressure level in the main gas path while increasing the pressure just inboard of the cavity rim, thus effectively reducing the potential for main gas ingestion.

72

Instantaneous velocity vector maps on the radial-azimuthal plane obtained at four axial locations in the rim cavity were discussed. At low purge air flow rate, the rim cavity flow was dominated by its tangential velocity component while the radial velocity component was nearly zero in the inboard half of the cavity. In the outboard half, the flow was either radially outward or inward depending upon the circumferential sector. As the purge air flow rate increased, more of radially inward flow was observed near the stator and more of radially outward flow near the rotor. The tangential velocity radial distribution became flat as the purge air flow rate increased.

Scrutiny of the static pressure, sealing effectiveness (Thiagarajan 2013) and PIV data led to the inference that a recirculation region was present in the rim cavity. The radial extent of this region expanded as the purge air flow rate increased. A sharp change in the radial velocity component from radially outward to inward was observed near the stator inner seal lip, this indicating that the rim cavity fluid entered the inner cavity here. This may explain the decrease in sealing effectiveness that was measured in the inner cavity as purge air flow rate increased. Such a trend may have been caused by unsteady low-pressure structures in the outermost region of the inner cavity.

4.2 Recommendations for Future Work

In the present experiments the radial location of the labyrinth seal in the disk cavity as well as the labyrinth seal gap was fixed. In order to further understand the influence of the labyrinth seal on the rim cavity flow, experiments should be performed by changing these parameters separately. For example, it

would be interesting to see the effect of changing in the radial location of the labyrinth seal on the size of the recirculation region in the rim cavity at varying purge air flow rates.

PIV velocity vector maps should also be obtained in the inner cavity. These maps will help ascertain whether there occurs radially inward flow of rim cavity fluid into the inner cavity at higher purge air flow rates. Unsteady pressure measurements should be carried out in the inner cavity to determine whether unsteady low-pressure structures are present in the inner cavity; this were believed to be the cause for the reduction in sealing effectiveness in the inner cavity at higher purge air flow rates.

Currently three-dimensional unsteady CFD simulations are being carried out for the given stage configuration. The computational results will complement the experimental results reported.

REFERENCES

Abe, T., Kikuchi, J., and Takeuchi, H., 1979, "An Investigation of Turbine Disk and Cooling (Experimental Investigation and Observation of Hot Gas Flow Into a Wheel Space)," Thirteenth CIMAC Congress, Vienna, Paper GT-30.

Adrian, R.J., 1991, "Particle-Imaging Techniques for Experimental Fluid Mechanics," Annual Review of Fluid Mechanics, Vol. 23, pp. 261-304.

Balasubramanian, J.H., 2010, "Experimental Study of Main Gas Ingestion and Purge Gas Egress Flow in Model Gas Turbine Stages," M.S., Thesis, Arizona State University.

Batchelor, G.K., 1951, "Note on a Class of Solutions of the Navier-Stokes Equations Representing Steady Rotationally-Symmetric Flow," Quart. J. Mech. Appl. Math., Vol. 4(1), pp. 29-41.

Bayley, F.J. and Owen, J.M., 1970, "Fluid Dynamics of a Shrouded Disk System with a Radial Outflow of Coolant," Journal of Engineering for Power, Vol. 92(3), pp. 335-341.

Bohn, D.E., Decker, A., Ma, H., and Wolff, M., 2003, "Influence of Sealing Air Mass Flow on the Velocity Distribution in and Inside the Rim of the Upstream Cavity of a 1.5-Stage Turbine," ASME Paper GT2003-38459.

Cao, C., Chew, J.W., Millington, P.R., and Hogg, S.I., 2003, "Interaction of Rim Seal and Annulus Flows in an Axial Flow Turbine," ASME Paper GT2003-38368.

Daily, J.W. and Nece, R.E., 1960, "Chamber Dimension Effects on Induced Flow and Frictional Resistance of Enclosed Rotating Disks," ASME J. Basic Eng., Vol. 82(1), pp. 217-232.

Gallier, K.D., Lawless, P.B., and Fleeter, S., 2000, "Investigation of Seal Purge Flow Effects on the Hub Flow Field in a Turbine Stage Using Particle Image Velocimetry," AIAA Paper 2000-3370.

Ganesan, S., 2007, "Flow Field in a Rotor-Stator Disk Cavity with and Without Pre-swirled Secondary Air," M.S., Thesis, Arizona State University.

Gentilhomme, O., Hills, N.J., Chew, J.W., and Turner, A.B., 2002, "Measurement and Analysis of Ingestion through a Turbine Rim Seal," ASME Paper GT2002-30481.

Green, T. and Turner, A. B., 1994, "Ingestion into the Upstream Wheelspace of an Axial Turbine Stage," ASME J. Turbomach., Vol. 116(2), pp. 327-332.
Johnson, B.V., Mack, G.J., Paolillo, R.E., and Daniels, W.A., 1994, "Turbine Rim Seal Gas Path Flow Ingestion Mechanisms," AIAA Paper 94-2703.

Johnson, B.V., Jakoby, R., Bohn, D.E., and Cunat, D., 2006, "A Method for Estimating the Influence of Time-Dependent Vane and Blade Pressure Fields on Turbine Rim Seal Ingestion," ASME Paper GT2006-90853.

Johnson, B.V., Wang, C.Z., and Roy, R.P., 2008, "A Rim Seal Orifice Model with 2 Cds and Effects of Swirl in Seals," ASME Paper GT2008-50650.

Junnarkar, N.U., 2010, "Experimental Study of the Flow Field in a Model 1.5-Stage Gas Turbine Rotor-Stator Disk Cavity," M.S., Thesis, Arizona State University.

Narzary, D., 2005, "Experimental Study of Flow Field in a Model Rotor-Stator Disk Cavity," M.S., Thesis, Arizona State University.

Owen, J.M. and Rogers, R.H., 1989, Flow and Heat Transfer in Rotating-Disc Systems. Vol. I: Rotor-Stator Systems, Research Studies Press, Taunton, United Kingdom.

Phadke, U.P. and Owen, J.M., 1983, "An Investigation of Ingress for an Air-Cooled Shrouded Rotating Disk System With Radial-Clearance Seals," J. Eng Power-T ASME, Vol. 105(1), pp. 178-182.

Phadke, U.P. and Owen, J.M., 1988, "Aerodynamic Aspects of the Sealing of Gas-Turbine Rotor-Stator Systems: Parts 1, 2 & 3," Int. J. Heat Fluid Fl., Vol. 9(2), pp. 98-117.

Roy, R.P., Devasenathipathy, S., Xu, G., and Zhao, Y., 1999, "A Study of the Flow Field in a Model Rotor-Stator Disk Cavity," ASME Paper 99-GT-246.

Roy, R.P., Xu, G., and Feng, J., 2000, "Study of Main-Stream Gas Ingestion in a Rotor-Stator Disk Cavity," AIAA Paper 2000-3372.

Roy, R.P., Xu, G., Feng, J., and Kang, S., 2001, "Pressure Field and Main Stream Gas Ingestion in Rotor Stator Disk Cavity," ASME Paper 2001-GT-564.

Roy, R.P., Feng, J., Narzary, D., and Paolollo, R.E., 2005, "Experiment on Gas Ingestion Through Axial-Flow Turbine Rim Seals," ASME J. Eng. Gas Turbines Power, Vol. 127(3), pp.573-582.

Roy, R.P., Zhou, D.W., Ganesan, S., Wang, C-Z., Paolollo, R.E., and Johnson, B.V., 2007, "The Flow Field and Main Gas Ingestion in a Rotor-Stator Cavity," ASME Paper GT2007-27671.

Thiagarajan, J.K., 2013, "Experimental Study of Pressure and Main Gas Ingestion Distributions in a Model Rotor-Stator Disk Cavity," M.S., Thesis, Arizona State University.

Wang, C.Z., Mathiyalagan, S.P., Johnson, B.V., Glahn, J.A., and Cloud, D.F., 2012, "Rim Seal Ingestion in a Turbine Stage from 360-Degree Time-Dependent Numerical Simulations," ASME Paper GT2012-68193.

Zhou, D.W., Roy, R.P., Wang, C.Z., and Glahn, J. A., 2011, "Main Gas Ingestion in a Turbine Stage for Three Rim Cavity Configurations," ASME J. Turbomach., Vol . 133(3), pp. 031023-1 - 031023-12.

APPENDIX A

CALIBRATION OF PIV SYSTEM

Calibration of the PIV system was done in order to determine whether the PIV setup could measure the velocity in the disk cavity accurately. The calibration test was carried out by focusing the camera and the light sheet on the rotor surface. Olive oil particles were injected into the secondary flow for a brief moment and then the oil valve was turned off. After sufficient time, the PIV experiment was carried out. The oil particles sticking on to the rotor surface due to the jet impingement effect of the labyrinth seal were seen in the images captured by the digital camera. These images were analyzed by TSI INSIGHT software. For the reported calibration experiment, the actual velocity of the oil particles sticking on to the rotor is purely tangential. Figure 2.13 shows the plot for the calibration experiment. The maximum mismatch between the experimental and actual value is 5.19%.
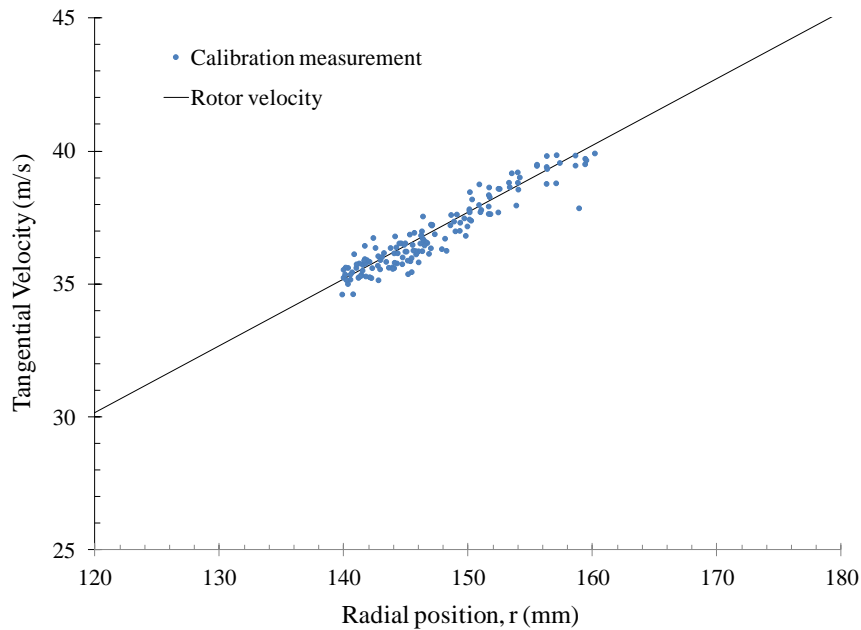

Fig. 2.13 Calibration of PIV system